

CHAPTER 2

FROM THE GAS PHASE TO A LIPID MEMBRANE ENVIRONMENT: DFT AND MD SIMULATIONS OF STRUCTURE AND DYNAMICS OF HYDROGEN-BONDED SOLVATES OF BIFUNCTIONAL HETEROAZAAROMATIC COMPOUNDS

ALEXANDER KYRYCHENKO¹ AND JACEK WALUK²

¹*V.N. Karazin Kharkov National University, Institute of Chemistry, 4 Svobody Sq., 61077, Kharkov, Ukraine,*

²*Polish Academy of Science, Institute of Physical Chemistry, Kasprzaka 44, 01-224, Warsaw, Poland,*

e-mail: waluk@ichf.edu.pl

Abstract: We present a review of our recent developments in computational modeling of hydrogen-bonding-induced phenomena in a series of biologically relevant bifunctional proton donor–acceptor heteroazaaromatic compounds. Different types of hydrogen-bonded solvates, in which water or alcohol molecules form a bridge connecting the proton donor (pyrrole NH group) and the acceptor (pyridine or quinoline nitrogen) atoms of bifunctional solutes, are explored by combining density functional theory (DFT) and molecular dynamics (MD) simulation approaches. Structure and dynamics of multiple hydrogen-bonded solute-solvent complexes are studied starting from isolated complexes in the gas phase, elucidating their solvation dynamics in solutions and, finally, in a heterogeneous environment of a lipid bilayer. Our results indicate that the structure, stoichiometry and hydrogen bond strength in such solvates are tuned by local topologies of the hydrogen-bonding sites of a bifunctional proton donor–acceptor molecule. A role of such solvates in hydrogen-bond-dependent photophysics and in controlling excited-state behavior of heteroazaaromatic compounds is discussed.

Keywords: Excited-state proton transfer, Hydrogen-bonded complexes, Hydrogen-bonded network, Density functional theory, TDDFT, Fluorescent probe, Lipid bilayer, Molecular dynamics simulations

2.1. INTRODUCTION

Heteroazaaromatic molecules containing both pyrrole/indole/carbazole and quinoline/pyridine heterocyclic units reveal complex spectroscopy and photophysics in hydroxylic solvents [1]. In such bifunctional compounds one moiety acts as a hydrogen bond donor, whereas the other plays a role of a hydrogen bond acceptor. The electronic excitation of such species can induce remarkable and cooperative acid–base changes, occurring on the opposite parts of an electronically excited chromophore. These changes provide a strong driving force for proton translocation from the NH donor moiety towards the accepting pyridine-type nitrogen atom [2]. If geometrical criteria are favorable, i.e., the donor and acceptor are hydrogen-bonded, such a proton transfer reaction can occur intramolecularly, as shown schematically in Figure 2-1a [3–7]. If it is not the case, the reaction can still occur; however, it now requires assistance of external hydrogen-bonding partners (Figure 2-1b) [8,9]. It has been demonstrated that in the presence of protic solvents, bifunctional hydrogen-bond donor–acceptor compounds are able to form cyclically hydrogen-bonded complexes with the solvent, in which solvent molecules act as a proton wire connecting the donor and acceptor parts of the chromophore. In such cyclically hydrogen-bonded solute–solvent complexes, solvent-assisted excited-state multiple proton transfer becomes possible [10–13].

One of the best known systems in this field is the dimer of 7-azaindole, for which the excited-state double proton transfer reaction was observed for the first time [14]. In such symmetric, doubly hydrogen-bonded system two possible, stepwise versus

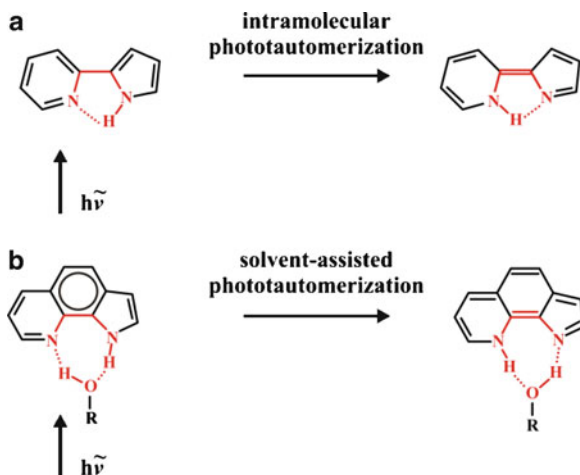


Figure 2-1. (a) Direct, intramolecular photoinduced proton-transfer tautomerization in 2-(2'-pyridyl)pyrrole. (b) Solvent-assisted proton-transfer reaction in a cyclic, hydrogen-bonded complex of 1*H*-pyrrolo[3,2-*h*]quinoline with a solvent molecule

concerted, proton transfer mechanisms have extensively been discussed [15–27]. Other interesting examples of bifunctional hydrogen-bond donor–acceptor molecules are provided by 6- and 7-hydroxyquinolines, in which migration of a proton occurs from a hydroxyl group towards a quinoline nitrogen atom via a solvent molecule bridge. It has been demonstrated that in 7-hydroxyquinoline proton transfer may proceed via solvent bridges composed of alcohols [28–30] or ammonia [31–37]. Proton translocation in 6-hydroxyquinoline has been shown to occur via a hydrogen-bonded molecular wire composed of two molecules of acetic acid [38, 39]. The excited-state multiple-proton relay along a hydrogen-bonded proton wire is believed to play an important role in the emitting mechanism of green fluorescent protein and many of its mutants [40–44]. Multiple proton migration in proton pump membrane proteins, such as bacteriorhodopsin, drives the proton transport across a biomembrane of a cell and it also proceeds through a proton wire acting against a pH gradient [45–47]. In many respects, these light-driven biological systems are also important for understanding the cooperative phenomena in proton conductivity and reorganization of the hydrogen-bonded networks.

Examples of several bifunctional molecules that have been studied with regard to structure and dynamics of hydrogen-bonded complexes are shown in Figure 2-2. While presenting our methodology and reviewing the results, we will focus mainly on 1H-pyrrolo[3,2-*h*]quinoline (PQ), a compound which has been investigated most extensively.

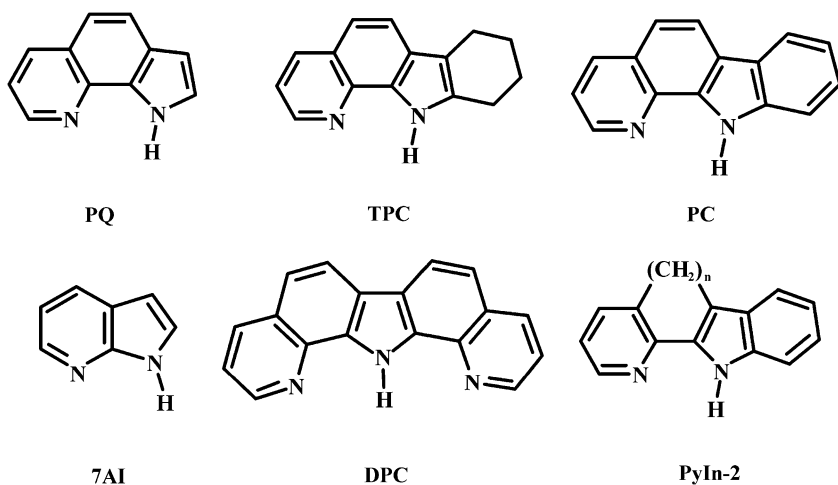


Figure 2-2. Structure of bifunctional hydrogen-bond donor/acceptor compounds: 1H-pyrrolo[3,2-*h*]quinoline (PQ), 7,8,9,10-tetrahydropyrido[2,3-*a*]carbazole (TPC), pyrido[2,3-*a*]carbazole (PC), 7-azaindole (7AI), dipyrido-[2,3-*a*: 3',2'-*i*]carbazole (DPC) and 2-(2'-pyridyl)indole, bridged by a chain consisting of two methylene units ($n = 2$, PyIn-2)

2.2. ELECTRONIC STRUCTURE OF 1H-PYRROLO[3,2-*h*]QUINOLINE

The ground-state (S_0) structure of PQ has been studied by means of the DFT method using the B3LYP hybrid functional and the correlation-consistent polarized valence cc-pVDZ basis set. Although valence excited states are of main interest, diffuse basis functions are required to calculate correctly low-lying Rydberg states, as well as $\pi\sigma^*$ excited states [48, 49]. Therefore, aug-cc-pVDZ basis functions are added on each of the two N1 and N4 nitrogen atoms and on the pyrrole hydrogen H5 of PQ (Figure 2-3a). Vertical electronic singlet and triplet excitation energies are

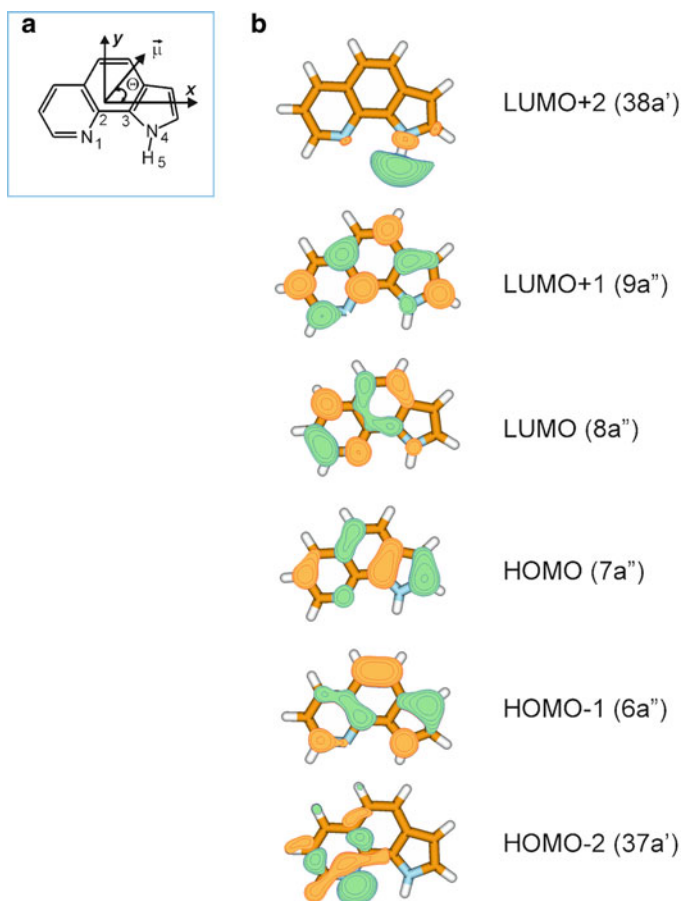


Figure 2-3. (a) Structure and atom labeling of PQ. The arrow defines a positive angle Θ of the direction of the excited-state transition moments and also, the ground and excited-state permanent dipole moments μ with respect to the long molecular axis x [50]. (b) Molecular orbitals involved in the low-lying electronic transitions of PQ

calculated for the S_0 -geometry of PQ applying the TDDFT methodology and using the same B3LYP functional and the basis set level of theory [50].

Figure 2-3b shows the molecular orbitals participating in the description of $S_0 \rightarrow S_i$ electronic transitions in the low-energy part of the absorption spectrum of PQ. Oscillator strengths, permanent/transition dipole moments and their directions, as well as main orbital configurations are summarized in Table 2-1. The energies of the two lowest electronic transitions, $S_0 \rightarrow S_1$ and $S_0 \rightarrow S_2$, are calculated at 3.89 and

Table 2-1 TD-B3LYP/cc-pVDZ results for isolated PQ: vertical excitation energies (eV), oscillator strengths (f), transition dipole moments (M, Debyes), transition moment directions ($\omega(M)$, degrees), permanent dipole moments (μ , Debyes), permanent dipole moment directions ($\Theta(\mu)$, degrees), and main electronic configurations [50] (Reproduced from [50] with permission from *Journal of Physical Chemistry*. A. Copyright © 2006 American Chemical Society)

State	TDDFT	Exp.	f	M	$\omega(M)$	μ	$\Theta(\mu)^a$	Main configuration (%)	
Singlet									
$1^1A'$						0.07	66.0		
$2^1A'$ ($\pi\pi^*$)	3.89 (3.52) ^b	3.66 ^c	0.0197	1.15	+52.1	4.57	−1.2	H→L H − 1→L + 1	85.8 9.1
$3^1A'$ ($\pi\pi^*$)	4.00	3.7–4.0 ^d	0.0304	1.42	−10.3	4.25	10.7	H − 1→L H→L + 1	80.8 15.0
$1^1A''$ ($n\pi^*$)	4.64	—	0.0020	0.33	^f	2.19	—	H − 2→L	98.7
$4^1A'$ ($\pi\pi^*$)	4.76	4.6–4.8 ^d	0.0795	2.09	+69.4	3.47	1.6	H − 1→L + 1 H→L	81.3 6.8
$5^1A'$ ($\pi\pi^*$)	4.95	4.6–4.8 ^d	0.4949	5.13	−6.4	2.11	−3.4	H→L + 1 H − 1→L	68.6 13.6
$2^1A''$ ($\pi\sigma^*$)	5.14	—	0.0020	0.30	—	12.38	—	H→L + 2	95.0
$3^1A''$ ($\pi\sigma^*$)	5.25	—	0.0012	0.24	—	13.65	—	H − 1→L + 2	94.8
$4^1A''$ ($n\pi^*$)	5.34	—	0.0001	0.05	^f	3.07	—	H − 2→L + 1	98.3
$6^1A'$ ($\pi\pi^*$)	5.60	—	0.1953	3.03	13.6	—	—	H − 3→L	63.3
Triplet									
$1^3A'$ ($\pi\pi^*$)	2.85	2.7 ^c	—	—	—	1.66	—	H→L H − 1→L	44.7 33.0
$2^3A'$ ($\pi\pi^*$)	3.36	—	—	—	—	4.17	—	H→L H − 1→L	40.4 52.3
$3^3A'$ ($\pi\pi^*$)	3.64	—	—	—	—	1.75	—	H→L + 1 H − 1→L + 1	62.0 19.0
$4^3A'$ ($\pi\pi^*$)	3.82	—	—	—	—	1.55	—	H − 1→L + 1 H→L + 1	66.0 25.7
$1^3A''$ ($n\pi^*$)	4.08	—	—	—	—	2.19	—	H − 2→L	93.8

^aSee Figure 2-3 for angle definition

^bZero-point energy corrected value for the energy gap between the $1^1A'$ and $2^1A'$ states

^c0-0 absorption band in supersonic jet [53]

^dAbsorption band maxima in *n*-hexane and 1-butanol [55]

^ePhosphorescence band maximum in 1-propanol and ethanol [55]

^fTransition moment directed along the out-of-plane *z* axis

4.00 eV, respectively. These vertical transitions correspond to $2^1A'$ and $3^1A'$ states. The vertical transition to the lowest excited state ($2^1A'$) has a small oscillator strength and its main electronic configuration (86%) is described by excitation from the highest occupied molecular orbital (HOMO) to the lowest unoccupied molecular orbital (LUMO). The excitation results in a significant intramolecular charge transfer from the pyrrole ring (HOMO) to the quinoline moiety (LUMO) (Figure 2-3b). The transition to the second ($3^1A'$) excited-state is described by the electronic configuration of HOMO-1→LUMO (81%). Similarly to $2^1A'$, this state is also characterized by a significant charge transfer character directed from the pyrrole towards the quinoline part of the chromophore. The S_1 and S_2 states are characterized by permanent dipole moments of 4.57 and 4.25 D, respectively. Comparison with the value of the ground-state dipole moment, 0.07 D, shows that, due to a charge transfer character, the $S_0 \rightarrow S_1$ and $S_0 \rightarrow S_2$ excitations result in a significant increase of the dipole moment of PQ. The $4^1A'$ and $5^1A'$ states are calculated to lie at 4.76 and 4.95 eV, respectively. These states have high oscillator strengths and they appear as a strong absorption band in the electronic spectrum (Figure 1 in reference [55]). The TDDFT calculation also predicts a forbidden electronic transition $1^1A' \rightarrow 1^1A''$ characterized by small oscillator strength of 0.002 and located at 4.64 eV. The orbital analysis indicates that this transition originates mainly from the HOMO-2→LUMO configuration and it may be assigned to an $n\pi^*$ state.

A pair of the $2^1A''$ and $3^1A''$ states is calculated to lie above $4^1A'$ and $5^1A'$. The electronic transitions to these states are described by electronic excitation from HOMO or HOMO-1 to a diffuse, Rydberg-type, LUMO+2 orbital (Figure 2-3b). The latter is of σ^* -type and it is localized on the pyrrole hydrogen atom. The $2^1A''$ and $3^1A''$ states can therefore be assigned as the $\pi\sigma^*$ excited states. The $\pi\sigma^*$ states have a very large excited-state dipole moment of about 12–13 D, as seen in Table 2-1.

The TDDFT-calculated properties of the two lowest excited states reveal evidence for their significant charge-transfer character. Therefore, acid and base properties of PQ in these excited-states are also expected to increase significantly, providing a driving force for the proton transfer reaction. $2^1A'$ and $3^1A'$ states are predicted to lie very close in energy to each other ($\Delta E \sim 0.11$ eV, Table 2-1). Since the TDDFT calculation are carried out for the gas phase, the ordering of these polar $2^1A'$ and $3^1A'$ states may be reversed in polar solutions. Additionally, it has been demonstrated that single-reference methods such as TDDFT tend to overestimate the energy of an excited-state with a multiconfigurational character by 0.2–0.4 eV [51]. The energy difference between $2^1A'$ and $3^1A'$ is in this overestimation range. Therefore, the low-energy part of the spectrum of PQ has been recalculated using the second-order coupled cluster method implemented with the resolution of the identity approximation (RI-CC2) [52]. This approach reproduces the same, $2^1A'$ and $3^1A'$, state ordering.

TDDFT calculations of the $S_0 \rightarrow S_n$ vertical excitation energies have shown a good agreement with the electronic absorption spectra measured in solution, as well as under jet-isolated conditions. The predicted energy of the lowest excited state S_1 ,

corrected for the zero-point energy terms, is 3.52 eV, which corresponds well with the 0-0 absorption band of 3.66 eV measured for the jet-isolated PQ [53]. The maximum of the strongest absorption band of PQ in *n*-hexane, assigned to the S_2 state, has been measured at about 3.9 eV, in good agreement with the value of 4.0 eV calculated by TDDFT [50].

2.3. STRUCTURE OF GAS-PHASE COMPLEXES

2.3.1. Hydrogen-Bonded Complexes with Water

Hydrogen bonding of PQ with water is considered for 1:1 and 1:2 PQ:water stoichiometries. In the case of 1:1, PQ forms a cyclic, hydrogen-bonded complex with water as shown in Figure 2-4 (center column). Such a complex, possessing two

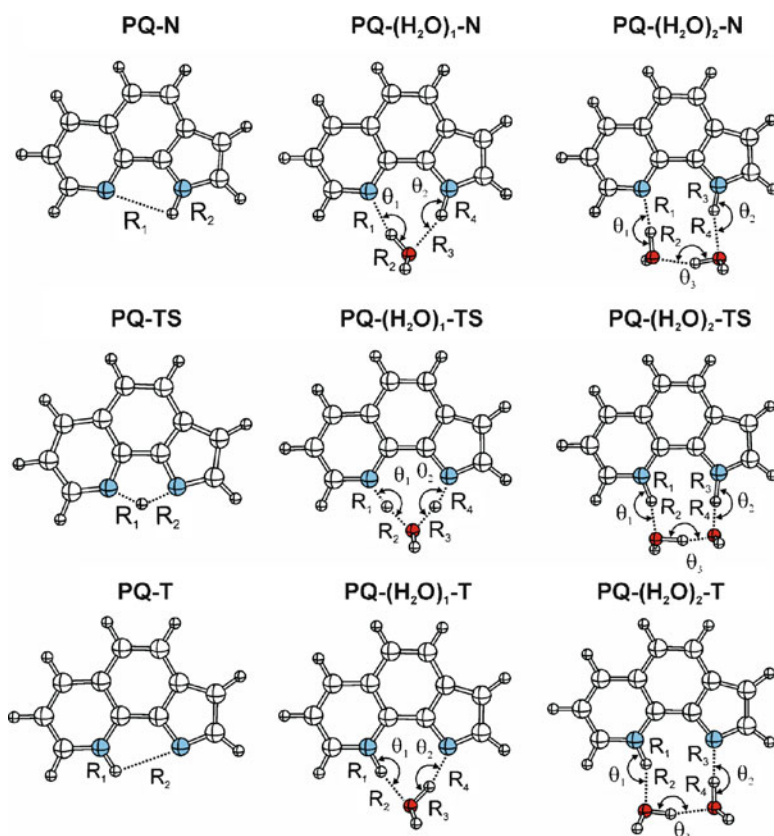


Figure 2-4. Geometry-optimized structures of the stationary points along the proton transfer reaction coordinate in bare PQ (left) as well as in PQ-(H₂O)₁ (center) and PQ-(H₂O)₂ (right). The proton-transfer relevant structural parameters are summarized in Table 2-2

hydrogen bonds, is calculated as the most energetically stable in the S_0 and S_1 states. The topology of the hydrogen-bond donor (NH) and hydrogen-bond acceptor (quinoline-type nitrogen) favors the formation of two almost linear hydrogen bonds characterized by very similar values of the H-bond lengths and angles, as shown in Table 2-2. The structure of $PQ-(H_2O)_1$ in the S_1 -state, optimized using the adiabatic TDDFT methodology [54], reveals that upon electronic excitation the two hydrogen bonds in $PQ-(H_2O)_1$ are strengthened compared to the situation in S_0 (Table 2-2).

In the case of 1:2 PQ:water stoichiometry, different types of hydrogen-bonded solvates are found. The first group of $PQ-(H_2O)_2$ complexes is generally characterized by a structure which is similar to that of the above-described 1:1 cyclically hydrogen-bonded form, $PQ-(H_2O)_1$. In this species, one water molecule forms a cyclic hydrogen-bonded structure with PQ, similarly as in $PQ-(H_2O)_1$, whereas the other water molecule is attached to the first one, acting as either an hydrogen bonding donor or as an acceptor. In terms of the photophysics of PQ, this set of hydrogen-bonded solvates is very similar to that of cyclic 1:1 $PQ-(H_2O)_1$ [53]. However, another type of 1:2 PQ:water complex was found to be energetically more stable. The most energetically favorable structure of $PQ-(H_2O)_2$ is shown in Figure 2-4 (right). In this structure, two water molecules form a cyclic, hydrogen-bonded chain connecting the pyrrole NH hydrogen and the quinoline-type nitrogen atom. The most relevant geometrical parameters of the H-bonded network in $PQ-(H_2O)_2$ are summarized in Table 2-2. The hydrogen bond lengths and angles

Table 2-2 Selected distances (R_i , Å) and angles (Θ_i , degrees) calculated for the stationary points (N – normal, TS – transition state, T – tautomer) along the proton transfer coordinate in $PQ-(H_2O)_n$ in the ground state (in brackets) and in the first excited singlet state [50] (Reproduced from [50] with permission from *Journal of Physical Chemistry A*. Copyright © 2006 American Chemical Society)

R_i and Θ_i	PQ			PQ-H ₂ O			PQ-(H ₂ O) ₂			
	N	TS	T	N	TS	T	N	TS _a	TS _b	T
R_1	2.63 (2.79)	1.34 (1.46)	1.01 (1.02)	1.67 (1.82)	1.26 (1.13)	1.02 (1.05)	1.67 (1.78)	1.14 (–)	1.02 (1.09)	1.02 (1.03)
R_2	1.01 (1.01)	1.26 (1.42)	2.55 (2.54)	1.02 (0.99)	1.24 (1.42)	1.89 (1.72)	1.02 (1.00)	1.38 (–)	1.94 (1.51)	1.95 (1.84)
R_3	–	–	–	1.73 (1.91)	1.44 (1.24)	0.99 (1.02)	1.03 (1.02)	1.09 (–)	1.15 (1.16)	1.77 (1.68)
R_4	–	–	–	1.04 (1.02)	1.12 (1.26)	1.80 (1.67)	1.79 (1.91)	1.51 (–)	1.34 (1.16)	1.00 (1.01)
Θ_1	–	–	–	165.7 (165.3)	167.3 (165.7)	167.9 (168.9)	175.6 (173.1)	171.0 (–)	153.7 (164.8)	154.4 (154.6)
Θ_2	–	–	–	156.1 (158.9)	158.7 (160.8)	160.1 (160.4)	162.1 (163.8)	169.1 (–)	175.3 (175.6)	177.4 (178.9)
Θ_3	–	–	–	–	–	–	162.3 (161.7)	167.3 (–)	160.8 (168.5)	163.2 (164.1)

in the cyclic H-bond network are found not to be equal, indicating the existence of some sterical strain in the PQ-(H₂O)₂ complex. The steric strain is partially reduced by out-of-plane rearrangement of the triple hydrogen-bonded chain, so that the oxygen atom of one of the water molecules is shifted below the molecular plane of PQ.

2.3.2. Excited-State Proton Transfer Through Water Bridges

The TDDFT analysis of the properties of PQ in the lowest excited singlet state reveals the evidence for the important role the charge-transfer type excitation may play in the excited-state behavior of the bifunctional heteroazaaromatic compounds. Our recent works on a number of bifunctional systems indicate that microsolvation involving hydrogen-bonding may trigger the excited-state translocation of proton from a proton-donating imino moiety to a proton-accepting pyridine-type nitrogen atom [1, 8, 9, 12]. Experimental spectroscopic studies have also shown that the phototautomerization is not the only excited state deactivation channel switched on by the formation of a hydrogen-bonded complex with a protic partner. Another channel is a rapid $S_0 \leftarrow S_1$ internal conversion [55]. The experiment suggests that the latter deactivation path is favored for 1:2 species, whereas 1:1 complexes undergo excited state proton transfer. We have examined the energetics and the potential energy profiles leading from the normal (N) form to the tautomer (T) via the transition state (TS) applying the adiabatic TDDFT method. In order to consider the proton transfer reaction path in PQ and PQ-(H₂O)_n solvates with $n = 1, 2$ geometries of PQ-N, PQ-TS and PQ-T stationary points were optimized for the S_0 and S_1 states. As shown in Figure 2-3a, in the normal form PQ-N, before the phototautomerization, the migrating proton H5 is attached to the pyrrole nitrogen atom N4. In the tautomeric form PQ-T, this proton becomes covalently attached to the nitrogen atom N1 of the quinoline-type moiety (Figure 2-4). The energy of the initial and final states of the reaction is summarized in Table 2-3, in which ΔE refers to the difference in total electronic energy between the corresponding stationary points. The energy of the normal form was set to zero. Table 2-3 also shows the enthalpy difference, ΔH_0 , which includes the zero point vibrational energy (ΔZPE) correction term to ΔE . In the S_0 state, in the absence of hydrogen-bonding with water, the PQ-N form is characterized by the lowest energy, corresponding to the global minimum on the S_0 potential energy surface. The energy of the ground state tautomer PQ-T is calculated to be higher than PQ-N by 18.6 kcal/mol in terms of ΔH_0 . In S_1 , however, the reversed energy ordering of PQ-N* and PQ-T* is observed. The TDDFT-optimized structure of PQ-T* is found to be most energetically stable, being lower in energy than PQ-N* by 16.4 kcal/mol. Thus, the TDDFT calculations demonstrate that the reaction $N^* \rightarrow T^*$ is strongly energetically favorable. Despite of the favorable energetics, the energy barrier to the intramolecular proton transfer is, however, found to be large. The barriers of 37.8 and 20.9 kcal/mol are calculated for S_0 and S_1 states, respectively. In the

Table 2-3 Proton transfer energetics (kcal/mol) for the stationary points calculated along the proton transfer reaction path in $\text{PQ}-(\text{H}_2\text{O})_n$. (Reproduced from [50] with permission from *Journal of Physical Chemistry A*. Copyright © 2006 American Chemical Society)

Structure	Stationary points	Energy (kcal/mol)			
		S_0 -state		S_1 -state	
		ΔE	ΔH_0	ΔE	ΔH_0
PQ	N	0.0	0.0	0.0	0.0
	TS	37.8	–	20.9	–
	T	21.0	18.6	–17.2	–16.4
$\text{PQ}-\text{H}_2\text{O}$	N	0.0	0.0	0.0	0.0
	TS	16.1	–	3.0	–
	T	14.6	12.7	–12.5	–11.8
$\text{PQ}-(\text{H}_2\text{O})_2$	N	0.0	0.0	0.0	0.0
	TS _a	17.8	–	5.6	–
	TS _b	–	–	1.5	–
	T	12.8	12.6	–12.0	–11.4

transition state PQ-TS^* , the geometry of the aromatic backbone of PQ is significantly distorted in comparison with the equilibrium structures PQ-N^* and PQ-T^* (Figure 2-4 and Table 2-2). The large energy barrier for the excited-state proton transfer reaction, estimated by TDDFT, is consistent with the spectroscopic results obtained in nonpolar and polar aprotic solvents. The fluorescence studies show that, due to the large activation energy, no photoinduced proton transfer is spectroscopically detected for PQ in the aprotic media [55].

The tautomerization energetics for the cyclic hydrogen-bonded complexes $\text{PQ}-(\text{H}_2\text{O})_n$ with one and two water molecules are presented in Table 2-3. In the case of the complex with one water, the TDDFT calculations show that the tautomeric form $\text{PQ}-(\text{H}_2\text{O})_1\text{-T}^*$ is lower in energy than $\text{PQ}-(\text{H}_2\text{O})_1\text{-N}^*$ by 12.5 kcal/mol in the S_1 state (Table 2-3). Thus, the formation of the cyclic hydrogen-bonded complex decreases the difference in the excited-state energy between $\text{PQ}-(\text{H}_2\text{O})_1\text{-N}^*$ and $\text{PQ}-(\text{H}_2\text{O})_1\text{-T}^*$. It is interesting that a more pronounced effect is observed for the energy barrier for the transfer of the proton from the pyrrole group to the quinoline nitrogen, assisted by the water molecule. In the cyclic complex, the steric strains within the hydrogen-bonded network are reduced, and this effect leads to the stabilization of the energy of the transition state structure $\text{PQ}-(\text{H}_2\text{O})_1\text{-TS}^*$, so that the barrier height for double proton transfer is reduced from 20.9 to 3.0 kcal/mol. Table 2-2 shows that when the system is passing the stationary point $\text{PQ}-(\text{H}_2\text{O})_1\text{-TS}^*$ the two protons move asynchronously. The water proton starts shifting to the quinoline-type nitrogen before the pyrrole proton detachment is initiated. The geometry of $\text{PQ}-(\text{H}_2\text{O})_1\text{-TS}^*$ indicates that this proton is located midway between the water oxygen and the quinoline nitrogen atom, as can be noticed from the distances R_1 and R_2 , equal to 1.26 and 1.24 Å, respectively

(Figure 2-4 and Table 2-2). The TDDFT calculations predict, therefore, that the phototautomerization in $\text{PQ}-(\text{H}_2\text{O})_1$ occurs by a concerted, asynchronous double proton transfer, which is assisted by a water molecule forming a hydrogen-bonded wire connecting the proton-donor and acceptor atoms of PQ.

A more complex proton transfer profile was found for the phototautomerization in $\text{PQ}-(\text{H}_2\text{O})_2$. Two transition states TS_a^* and TS_b^* were identified along the excited-state reaction path connecting $\text{PQ}-(\text{H}_2\text{O})_2-\text{N}^*$ and $\text{PQ}-(\text{H}_2\text{O})_2-\text{T}^*$. The order of the TS_a^* and TS_b^* transition states on the pathway from the initial N^* state to the final T^* state is mainly determined by the structural similarity of TS_a^* and TS_b^* to either N^* or T^* . As can be seen from Table 2-2, the values of the hydrogen bond lengths R_3 and R_4 in TS_a^* ($R_3 = 1.09 \text{ \AA}$ and $R_4 = 1.51 \text{ \AA}$) are closer to those of the initial state N^* ($R_3 = 1.03 \text{ \AA}$ and $R_4 = 1.79 \text{ \AA}$) rather than to the final state T^* ($R_3 = 1.77 \text{ \AA}$ and $R_4 = 1.00 \text{ \AA}$). The structural difference between N^* and TS_a^* is located, therefore, in different values of R_1 and R_2 . Upon going from N^* to TS_a^* , R_1 and R_2 are rearranged from $R_1 = 1.67 \text{ \AA}$ and $R_2 = 1.02 \text{ \AA}$ (in N^*) to $R_1 = 1.14 \text{ \AA}$ and $R_2 = 1.38 \text{ \AA}$ (in TS_a^*). This structural transformation corresponds to the transfer of one proton from the water molecule to the nitrogen atom of the quinoline ring of PQ. In TS_a^* , the other two protons involved in tautomerization are still connected to the corresponding heavy atoms. On the other hand, the structure of the TS_b^* state is closer to that of the final state T^* , because R_1 and R_2 are similar in both TS_b^* ($R_1 = 1.02 \text{ \AA}$ and $R_2 = 1.94 \text{ \AA}$) and T^* ($R_1 = 1.02 \text{ \AA}$ and $R_2 = 1.95 \text{ \AA}$). That means that in order to reach the TS_b^* state directly, the system should already have R_1 and R_2 rearranged, but this R_1 and R_2 rearrangement is actually passing through TS_a^* . Based on these considerations, the phototautomerization in $\text{PQ}-(\text{H}_2\text{O})_2$ proceeds as $\text{N}^* \rightarrow \text{TS}_a^* \rightarrow \text{TS}_b^* \rightarrow \text{T}^*$. The first state TS_a^* is characteristic for highly asynchronous concerted proton movement along the hydrogen-bonded network (Table 2-2). In this state, the transfer of one proton from the oxygen atom of the first water to the quinoline nitrogen atom becomes almost complete, whereas the other two transferring protons are still attached to the pyrrole nitrogen and the oxygen atom of the second water, respectively. In the case of the second transition state TS_b^* , one proton is moved from the water molecule and becomes attached to the quinoline nitrogen, whereas the pyrrole hydrogen only starts moving towards the water dimer. The ΔE barriers between the initial form, $\text{PQ}-(\text{H}_2\text{O})_2-\text{N}^*$ and the corresponding transition states, $\text{PQ}-(\text{H}_2\text{O})_2-\text{TS}_a^*$ and $\text{PQ}-(\text{H}_2\text{O})_2-\text{TS}_b^*$ are calculated to be 5.6 and 1.5 kcal/mol, respectively. Thus, the first transition state determines the overall rate for the triple proton transfer in $\text{PQ}-(\text{H}_2\text{O})_2$. The analysis of bond lengths and angles in the hydrogen-bonded network of $\text{PQ}-(\text{H}_2\text{O})_2$ connecting the hydrogen-bond donor and acceptor atoms indicates that the complete tautomerization is not able to proceed by simultaneous and cooperative transfer of the three protons. This type of multiple proton transfer along a hydrogen-bonded proton wire has been reported for the transfer via hydrogen-bonded water bridges composed of equivalent or similar hydrogen bonds [56–60]. Such concerted reorganization of a hydrogen-bonded network may proceed via cooperative breaking and re-forming of hydrogen bonds possessing very similar geometry. It has also

been reported that the cooperative transfer may be blocked in the case of unfavorable geometry of one of hydrogen-bonds participating in a bridge [61–64]. The significant nonequivalence of the three hydrogen bonds in $\text{PQ}-(\text{H}_2\text{O})_2-\text{N}^*$ leads to strongly asynchronous movement of the two transferring protons. The triple proton transfer occurs, therefore, in a step-by-step fashion through $\text{PQ}-(\text{H}_2\text{O})_2-\text{TS}_a^*$ and $\text{PQ}-(\text{H}_2\text{O})_2-\text{TS}_b^*$, which requires a significant rearrangement of the positions of heavy oxygen atoms of the water cluster. This asynchronous transfer leads to the situation when, at a certain time, only one hydrogen bond is broken along the hydrogen-bonded bridge. After this single proton transfer step, the hydrogen-bonded network is being rearranged and, after that, the transfer of the second proton requires less activation energy. Therefore, we found that even though tautomerization in $\text{PQ}-(\text{H}_2\text{O})_2$ is possible, it requires large relaxation and reorganization of the hydrogen-bonded water bridge. This reorganization may, therefore, trigger the excited state depopulation of PQ via internal conversion and thus block the complete tautomerization in this type of microsolvates.

2.3.3. Hydrogen-Bonded Complexes with Methanol

The hydrogen-bonded complexes of 7-azaindole (7AI, Figure 2-2) with protic solvent molecules have previously been investigated at various levels of theory [65]. The ground-state structure of 7AI complexes with the smallest protic solvent, water, have been studied in detail, including such methods as DFT [66, 67] and MP2 [68]. The excited-state structure and properties of $7\text{AI}-(\text{H}_2\text{O})_n$ have been evaluated using ab initio approach employing a configuration interactions scheme (CIS), involving single excited configurations [69–72], as well as high level multi-configurational schemes such as MCSCF [73] and CASSCF [74]. Recently, geometries, electronic structure, excited-state permanent dipole moments, as well as the orientations of transition dipole moments in $7\text{AI}-(\text{H}_2\text{O})_n$ clusters have been re-evaluated using robust, second-order approximated coupled cluster model within the resolution-of-the identity approximation (RI-CC2) [75,76]. The RI-CC2 structure calculations combined with laser-induced fluorescence experiments have also been reported for jet-cooled clusters of 7AI with ammonia [77]. Sekiya and coworkers have applied supersonic jet-cooled fluorescence experiments combined with quantum chemistry calculations to study the structures of microsolvated clusters of 7AI with methanol molecules. They reported the ground-state structures of $7\text{AI}-(\text{MeOH})_n$ with $n = 2, 3$ and the excited state proton transfer reaction path calculations carried out at MP2/6-31++G** and CIS/6-31++G** levels, respectively [62,78]. The structure and the reaction path for the proton transfer have also been reported for 7AI/carboxylic acid complexes calculated at Hartree-Fock/DFT [79] and CIS levels [80]. These computational studies have shown that the structure and proton transfer photoreactivity of hydrogen-bonded complexes of 7AI with various protic partners are strongly dependent on the structural topology of solute/solvents hydrogen-bonding centers.

Here we have compared the ground-state structure of methanol complexes of 7AI with those of two other bifunctional compounds, PQ and PyIn-2 (Figure 2-2). In the latter ones, the topology of hydrogen-bonding sites differs from that of 7AI. The structure of hydrogen-bonded complexes with one and two methanol molecules studied at the B3LYP/6-31G(d,p) level is presented in Figure 2-5. Hydrogen-bond lengths and angles are summarized in Table 2-4. All three solutes form two kinds of solute-solvent complexes with methanol: a π -complex and a hydrogen-bonded

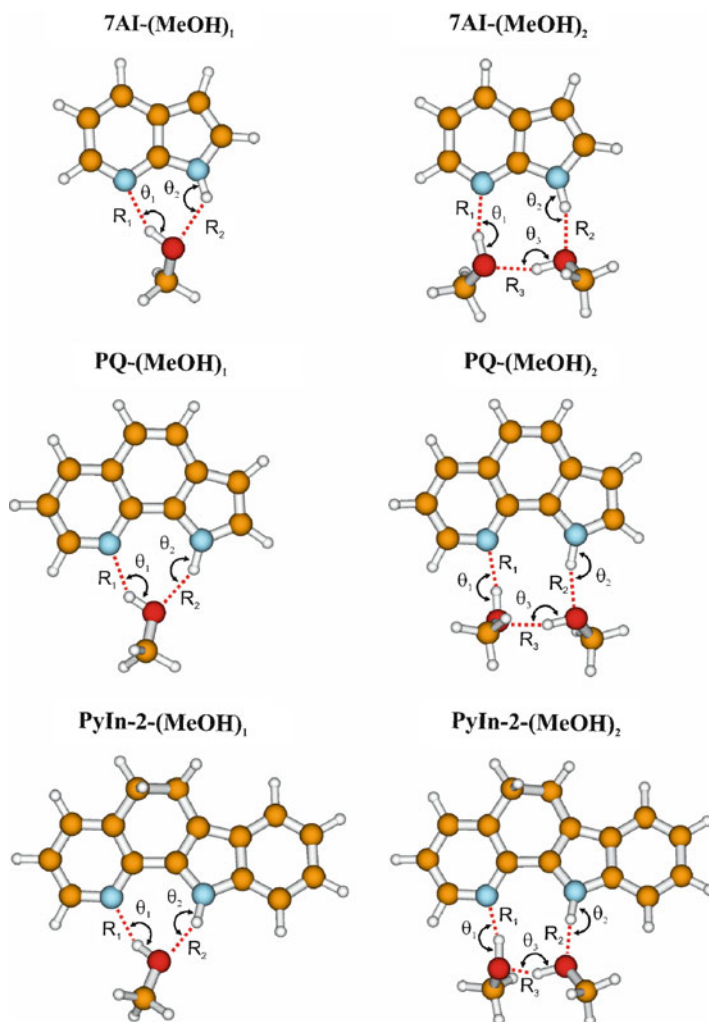


Figure 2-5. B3LYP/6-31G(d,p) optimized geometries of 1:1 and 1:2 cyclic hydrogen-bonded complexes of 7AI, PQ and PyIn-2 with methanol [83–85]. The most important hydrogen-bond structural parameters (R_i and Θ_j) are collected in Table 2-4

Table 2-4 Selected hydrogen bond lengths (R_i , Å) and angles (Θ_i , degrees) for methanol complexes of 7AI-(MeOH) $_n$, PQ-(MeOH) $_n$ and PyIn-2-(MeOH) $_n$ with $n = 1, 2$ calculated at the B3LYP/6-31G(d,p) level [83]

Hydrogen-bond parameters	7AI		PQ		PyIn-2	
	7AI + 1 MeOH	7AI + 2 MeOH	PQ + 1 MeOH	PQ + 2 MeOH	PyIn-2 + 1 MeOH	PyIn-2 + 2 MeOH
R_1	1.95	1.81	1.84	1.79	1.85	1.79
R_2	2.00	1.79	1.84	1.85	1.87	1.84
R_3	–	1.72	–	1.72	–	1.74
Θ_1	149.7	170.8	163.2	170.4	164.1	172.7
Θ_2	136.2	172.3	157.5	162.5	158.6	166.6
Θ_3	–	165.1	–	164.8	–	159.7
ΔE^a	–7.8	–18.4	–9.9	–15.1	–8.1	–14.8
	–8.5 ^b	–17.4 ^b				
	–9.2 ^c					
ΔH^d	–6.3 \pm 1.5 ^e	–	–9.2 \pm 0.7 ^f	–	–8.7 \pm 0.2 ^g	–

^aBinding energy in kcal/mol

^bCalculated at the MP2/6-31++G** level with applying BSSE and ZPE corrections [78]

^cCalculated at the HF/6-31G* level with no BSSE corrections [81]

^dExperimental binding enthalpy in kcal/mol

^eMethanol complex in cyclohexane [81]

^fComplex with *n*-butanol in *n*-hexane [55]

^gMethanol complex in *n*-hexane [82]

complex. The most stable structures are found to be hydrogen-bonded species. For all three solutes, the geometry optimization of a hydrogen-bonded complex with a 1:1 stoichiometry has always been converging to a cyclic, $NH \cdots OH \cdots N$, double hydrogen-bonded structure, as shown in Figure 2-5 (left column). The structural analysis of 1:1 methanol complexes has shown that in PQ-(MeOH) $_1$ and PyIn-2-(MeOH) $_1$ the two hydrogen bonds, characterized by Θ_1 and Θ_2 angles, as indicated in Figure 2-5 and Table 2-4, are more linear than those in 7AI-(MeOH) $_1$. On the basis of simple electrostatic and hybridized valence bond considerations a linear hydrogen-bond is expected to be energetically preferred, so that the strength of hydrogen-bonding association is well correlated with simple hydrogen-bonding geometrical parameters, such as the $X-H \cdots Y$ bond length and angle. Table 2-4 shows that the largest deviations from the idealized hydrogen-bonded geometry within the series of the 1:1 solute-methanol complexes are observed for 7AI-(MeOH) $_1$. The geometrical criteria for the hydrogen bond strength in the 1:1 complexes also correlate well with the energy of their formation, ΔE , calculated at the same B3LYP/6-31G(d,p) level and corrected for zero-point energy (ZPE) and basis set superposition error (BSSE) contributions (Table 2-4). The energy of the formation of the 1:1 complex has been calculated as 7.8, 8.1 and 9.9 kcal/mol for 7AI-(MeOH) $_1$, PyIn-2-(MeOH) $_1$, and PQ-(MeOH) $_1$, respectively. Thus, it has been concluded that PQ forms the strongest hydrogen-bonded complex with methanol, whereas the hydrogen-bonding

in 7AI-(MeOH)₁ is the weakest among the three studied compounds. The DFT-computed binding energies are also in good agreement with the experimentally determined enthalpies of hydrogen-bonding association, ΔH (Table 2-4). Chou and co-authors have reported the enthalpy of the formation of the hydrogen-bonded complex between 7AI and one methanol molecule in a cyclohexane solution as -6.3 ± 1.5 kcal/mol [81]. For the hydrogen-bonding association between PyIn-2 and methanol in *n*-hexane solution the enthalpy is -8.7 ± 0.2 kcal/mol [82]. Using spectroscopic titration methods, we have estimated the enthalpy for the association reaction between PQ and one *n*-butanol molecule in *n*-hexane solution as -9.2 ± 0.7 kcal/mol [55]. Therefore, both experimental and theoretical findings have provided substantial evidence that the hydrogen-bonding strength decreases in the following sequence: PQ-(MeOH)₁ > PyIn-2-(MeOH)₁ > 7AI-(MeOH)₁.

In the case of 1:2 solute-methanol complexes, a cyclic, triply hydrogen-bonded complex containing two methanol molecules, bound in a closed OH hydrogen-bonded network, has been found as the most stable structure compared to other possible hydrogen-bonded configurations for all three bifunctional solutes, as shown in Figure 2-5. Table 2-4 demonstrates that, in contrast to 7AI-(MeOH)₁, in the case of 7AI-(MeOH)₂ two hydrogen bond angles Θ_1 and Θ_2 have approached the values which are close to the ideal hydrogen-bond angle of 180°. The hydrogen bond lengths in the triple bound “eight-membered ring” structure of 7AI-(MeOH)₂ have become shorter than those in 7AI-(MeOH)₁, indicating the increase in the hydrogen bond strength in the former complex. Hydrogen bonds in cyclic “nine-membered ring” structures of PQ-(MeOH)₂ and PyIn-2-(MeOH)₂ have also rearranged toward the idealized hydrogen bond parameters. Despite of an overall increase in the hydrogen bonding strength among the 1:2 solute-methanol complexes, the opposite tendency has been observed in the binding energy for the 1:2 cyclic, triply hydrogen-bonded complexes than that obtained for the 1:1 hydrogen-bonded solvates. As can be seen in Table 2-4, the B3LYP/6-31G(d,p) binding energies are 15.1, 14.8 and 18.4 kcal/mol for PQ-(MeOH)₂, PyIn-2-(MeOH)₂ and 7AI-(MeOH)₂, respectively. Thus, 7AI-(MeOH)₂ has been found to form the most stable complex among the three studied bifunctional solutes. The larger exothermicity of the complex formation of 7AI-(MeOH)₂ can be explained by the possibility of the adjustment of the hydrogen bond distances and angles within the triple hydrogen-bonded solvent wire toward an idealized wire configuration, in which each N-H···O and N···H-O bonds would be almost linear.

We have also re-evaluated the ground-state structure and normal vibrational modes of PQ-(MeOH)_n using more precise ab initio methodology based on the resolution of identity (RI) method combined with the MP2 procedure referred to as RI-MP2/TZVP [86, 87]. Applying the TDDFT methodology described in Section 2.3.1 for PQ-(H₂O)_n solvates, we have studied the influence of the $S_1 \leftarrow S_0$ electronic excitation on the structure of hydrogen-bonded complexes in the lowest singlet-excited state at the TD-B3LYP/cc-pVDZ level. Crucial hydrogen bond parameters for PQ-(MeOH)_n with $n = 1, 2$ are summarized for both the S_0 and S_1 states in Table 2-5. Our DFT and RI-MP2 studies on the structure and

Table 2-5 Selected hydrogen bond lengths (R_i , Å) and angles (Θ_i , degrees) for methanol complexes of PQ–(MeOH) $_n$ with $n = 1, 2$ in the S_0 and S_1 states calculated at the B3LYP/cc-pVDZ level [85]. The hydrogen bond parameters for the S_0 state are also compared with the RI-MP2/TZVP data

Hydrogen-bond parameters	PQ + 1 MeOH			PQ + 2 MeOH		
	MP2		S_1	MP2		S_1
	S_0	DFT S_0		S_0	DFT S_0	
R_1	1.84	1.83	1.68	1.79	1.80	1.72
R_2	1.87	1.88	1.71	1.77	1.87	1.73
R_3	–	–	–	1.76	1.74	1.67
Θ_1	162.5	165.3	164.8	174.7	174.5	176.8
Θ_2	157.5	156.8	159.1	173.1	166.0	166.8
Θ_3	–	–	–	154.6	162.4	163.4
ΔE	–	–10.4	–	–	–13.9 ^a	–

^aThe binding energy was estimated for the binding interaction between PQ and a hydrogen-bonded methanol dimer, so that ΔE does not include a contribution of methanol-methanol hydrogen-bonding, which was calculated to be –3.9 kcal/mol at the same level of theory

hydrogen-bonding interactions of PQ with one and two methanol molecules have shown that even DFT calculations with medium size basis sets are entirely sufficient to provide a correct picture of hydrogen bond structures of PQ, which is evident from comparison with the structures obtained by the more accurate RI-MP2 method (Tables 2-4 and 2-5). As it was described in Section 2.2, the $S_1 \leftarrow S_0$ electronic transition is accompanied by the intramolecular charge transfer from the pyrrole ring toward the quinoline moiety. Therefore, the electronic excitation should result in an overall strengthening of the solute–solvent hydrogen-bonding in the S_1 -state. This hydrogen bond strengthening in S_1 has indeed been observed for both PQ–(MeOH) $_1$ and PQ–(MeOH) $_2$, as can be noticed from Table 2-5.

2.3.4. Cluster Size Effect on Fluorescence Quenching in Hydrogen-Bonded Complexes of PQ with Methanol

It has recently been found that, in the gas phase, photophysical properties of PQ depend strongly on stepwise microsolvation by methanol molecules [84]. In particular, no laser-induced fluorescence (LIF) has been observed for the jet-cooled PQ–(MeOH) $_1$, while strong LIF signals were detected for PQ–(MeOH) $_2$ and its larger size methanol clusters. In PQ–(MeOH) $_2$, the emission was characterized by a structured excitation spectrum up to excess energies of 663 cm^{–1}, above which the LIF spectra were vanishing [85]. The difference in the LIF behavior for PQ–(MeOH) $_n$ clusters with different sizes indicates the existence of a fast relaxation channel in PQ–(MeOH) $_1$ which is not observed in PQ–(MeOH) $_2$. Further

detection and characterization of PQ–methanol clusters by measuring their infrared (IR) spectra in the N–H and O–H stretch regions using femtosecond multiphoton ionization (fsMPI) methodology have allowed to observe a short-lived PQ–methanol complex which was not originally detected using nanosecond laser excitation. Based on IR/fsMPI spectrum and DFT vibrational frequency calculations, the complex possessing a short excited-state lifetime has been assigned to a cyclic, double hydrogen-bonded complex of PQ with one methanol molecule, the structure of which may schematically be outlined as PQ–(MeOH)₁ in Figure 2-5 [84]. It has been proposed that the short lifetime of the excited state of PQ–(MeOH)₁ is due to a rapid double proton transfer reaction which is followed by nonradiative relaxation. It is interesting that, using the mass-resolved vibronic and the dispersed fluorescence spectra, Sekiya and co-authors have recently observed the photoinduced proton/hydrogen atom relay for supersonically cooled 7AI–(MeOH)₂, but not for 7AI–(MeOH)₁ [62]. These experimental findings correlate well with our DFT-based conclusions that, in the gas phase, the formation of 7AI–(MeOH)₂ is more favorable than of 7AI–(MeOH)₁. The former is characterized by the cyclic, triple hydrogen-bonded structure with close-to-ideal hydrogen bond network. In PQ, the two almost perfect hydrogen bonds are formed already in the case of PQ–(MeOH)₁, so that the formation of the cyclic, triply hydrogen-bonded structure in PQ–(MeOH)₂ introduces some steric perturbations in the hydrogen-bonded OH network. The cluster size effect on the excited-state proton transfer reaction, which is being driven by an electron transfer along the ammonia wire, has also been reported by Leutwyler and coworkers for 7-hydroxyquinoline (7HQ)–ammonia clusters [33,88]. In addition, combining the fluorescence-detected IR spectra in the OH stretching region and DFT-based normal mode analysis, Matsumoto and coworkers have also found that, similarly to ammonia, at least three molecules of methanol are required to form a jet-cooled 7HQ–(MeOH)₃ cluster, in which the photoinduced keto-enol tautomerization of 7HQ starts to appear [30].

2.4. HYDROGEN BONDING OF HETEROAZAAROMATICS IN SOLUTION

Bifunctional H-bond donor–acceptor molecules, such as 7AI and PQ, exist in bulk alcohol or water solvents in a wide range of hydrogen-bonded species. Only a selected fraction of the equilibrium population possesses an appropriately hydrogen-bonded structure, able to tautomerize directly and rapidly after electronic excitation [55]. The detailed structure of such a phototautomerization precursor is, however, difficult to determine in bulk solution. To minimize the effect of solvent self-aggregation, the dilution of a small amount of alcohol or water in non-polar hydrocarbon solvents may be considered [55, 89]. Solvation dynamics and hydrogen bonding of 7AI, PQ and PyIn-2 in bulk alcohol or water solutions, as well as in *n*-hexane solution containing only one and two molecules of these

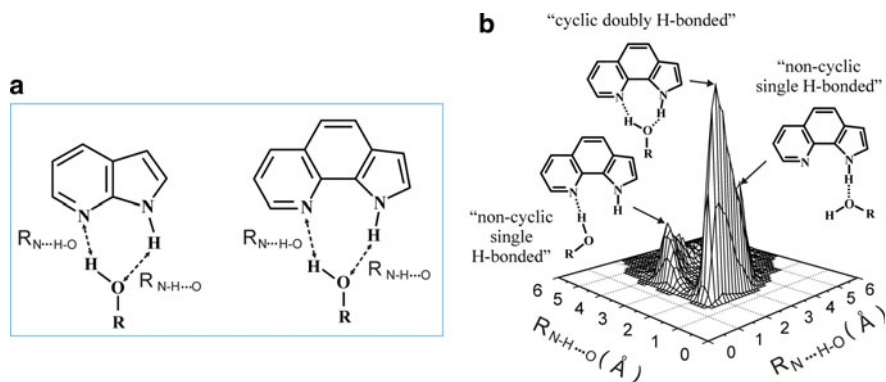


Figure 2-6. (a) The definition of two hydrogen-bonding parameters, $R_{N-H\cdots O}$ and $R_{N\cdots H-O}$, in 1:1 cyclic complexes of 7AI and PQ with protic solvents. (b) An example of a hydrogen-bonding distance distribution (HBD) displaying a relative frequency of a simultaneous occurrence of a pair of distances simulated for PQ in *n*-hexane in the presence of two methanol molecules. Populations of different kinds of hydrogen-bonded solvates of PQ, involving cyclic and non-cyclic H-bonded species, can be reconstructed from a 3D representation of an HBD distribution. Both $R_{N-H\cdots O}$ and $R_{N\cdots H-O}$ distances are calculated at every step during MD simulations; however, the corresponding H-bond values are included in the HBD distribution only when both H-bond distances are simultaneously found to be smaller than the cutoff of 7 Å

solvents, have been explored by classical molecular dynamics simulations using the GROMOS96 package of programs [83,90].

The bifunctional compounds possess two centers able to form hydrogen bonds with the solvent, acting either as a donor or an acceptor. Hydrogen bond definition and geometrical criteria for 7AI and PQ are shown in Figure 2-6a. The hydrogen bond between the pyridine-type nitrogen atom of the solute and the hydrogen atom of hydroxylic solvents (alcohol or water) is labeled as “N \cdots H-O”, while that between the hydrogen atom of the pyrrole NH group and the solvent oxygen atom is referred to as “N-H \cdots O”. During MD simulations, the solute-solvent hydrogen bonding is analyzed in terms of hydrogen-bonding distance distribution (HBD distribution), which displays a relative frequency of a simultaneous occurrence of a pair of $R_{N-H\cdots O}$ and $R_{N\cdots H-O}$ distances within hydrogen-bonded complexes, as shown in Figure 2-6b. Such 3D representation of hydrogen-bonding allows one to reconstruct structures and populations of different kinds of H-bonded complexes between the solute and surrounding solvent molecules, accumulated and averaged over a long MD simulation period.

2.4.1. Hydrogen-Bonded Complexes with Methanol and Water

The details of the MD simulations have been presented in reference [83]. Briefly, the simulation was based on a classical MD approach implemented in the GROMOS96 program package [90]. The 43A1 force field was used for modeling

bulk solvent and solvent mixtures, whereas the corresponding force field and charges for the azaaromatics were developed from the gas-phase B3LYP/6-31+G(d,p) structure calculations. The simulations were performed using periodic boundary conditions at the constant number of particles, constant pressure of 1 atm, and constant temperature of 300 K. The simulated systems included 116 and 216 solvent molecules for *n*-hexane, and methanol or water, respectively.

The HBD distributions for 1:1 complexes of 7AI, PQ and PyIn-2 in *n*-hexane solution in the presence of one methanol molecule are shown in Figure 2-7 (top). The distribution is characterized by one peak in which the most probable values of a pair of both hydrogen bond distances span a narrow range from 1.9 Å to about 2.5 Å. The population of hydrogen-bonded species, which may be described by such a kind of hydrogen bonding, corresponds to a complex in which, most of the time, a single methanol molecule is simultaneously H-bonded to both H-bonding donor and acceptor atoms of the solute. The structure and hydrogen bond lengths of such a solvate conform to a cyclic, doubly hydrogen-bonded complex between the solute and one methanol molecule, as shown schematically for a cyclic 1:1 PQ–water complex in Figure 2-6b. The comparison between 7AI, PQ and PyIn-2 shows that in the cases of PQ and PyIn-2 a cyclic, doubly hydrogen-bonded complex has a more “rigid” structure than the analogous cyclic species of 7AI. In the latter case, a fraction of the H-bonded species with one of the distances exceeding the maximum cutoff value of 2.5 Å for H-bonding is observed. Therefore, in such a cyclic solvate of

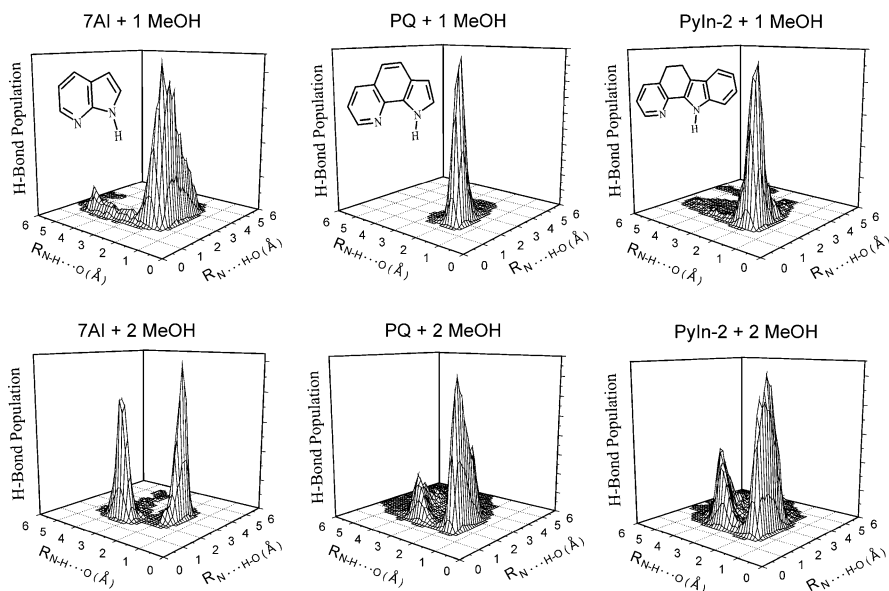


Figure 2-7. The HBD distributions for 7AI, PQ and PyIn-2 simulated for *n*-hexane in the presence of one (top) and two (bottom) molecules of methanol [83]

7AI, one of the two hydrogen-bonds periodically becomes broken. Applying the two cutoff criteria of 2.5 and 2.2 Å for weak and strong hydrogen bonds, respectively, a relative equilibrium population of the cyclic complexes may be estimated. For 7AI-(MeOH)₁, the equilibrium fractions of the cyclic complexes are 37% and 13%, respectively. Thus, only for about 13–37% of the time, 7AI is solvated in a “cyclic manner” and, for the rest of the time, one of the two hydrogen bonds, the N···H–O, is broken more frequently than the N–H···O bond. Such analysis can be used to reconstruct the average structure and hydrogen bonding dynamics for PQ-(MeOH)₁ and PyIn-2-(MeOH)₁. Populations of the complexes, their average hydrogen bond lengths and relative strength, estimated as the full width at half-maximum (*fwhm*) of the corresponding HBD distribution peak, are summarized in Table 2-6. As can be seen, in the case of PQ-(MeOH)₁, the cyclic complex is observed to persist for 69–88% of the simulation time depending on the hydrogen bond cutoff criteria. PyIn-2-(MeOH)₁ is found to be an intermediate case between 7AI and PQ in terms of the equilibrium population of the cyclic species, 50–72%, respectively.

Addition of a second methanol molecule to 7AI-(MeOH)₁ complex changes the hydrogen bonding pattern in a new formed 7AI-(MeOH)₂ solvate dramatically (Figure 2-7, bottom left). In the HBD distribution, the single peak corresponding to the 1:1 cyclic complex has disappeared and two new peaks have appeared. This new solvation structure conforms to the complex in which each methanol molecule is strongly hydrogen-bonded to only one of the two centers of H-bonding of the solute. In addition, the two methanol molecules are hydrogen-bonded to each other, forming a triply hydrogen-bonded wire connecting the pyrrole hydrogen (NH) and pyridine-type nitrogen of 7AI. Thus, a cyclic, doubly hydrogen-bonded complex in 7AI becomes unfavorable when more than one methanol molecule is present in solution. The fraction of the cyclic 1:1 species decreases below 1% (Table 2-6). In this context it is interesting that, as already mentioned, a recent supersonic jet study of 7AI-(MeOH)_n clusters has demonstrated the presence of 1:1, 1:2 and 1:3 hydrogen-bonded complexes, among which the phototautomerization was only observed in the 1:2 species [62]. In the cases of PQ-(MeOH)₂ and PyIn-2-(MeOH)₂, a different MD picture is observed when a second methanol molecule becomes available. The addition of the second methanol molecule only leads to some broadening of the major peak in the HBD distribution. In the case of PQ-(MeOH)₂, about 26–39% of the hydrogen-bonded species still correspond to the 1:1 cyclic, doubly hydrogen-bonded complex. The appearance of a small population of non-cyclic hydrogen-bonded species is seen as two minor peaks in the HBD distribution. In PyIn-2-(MeOH)₂, the same pattern of three H-bonded complexes is found, and the cyclic complex is present for about 15–26% of the time. Solute-solvent solvates with higher solvent stoichiometry, up to 1:5, show that the addition of subsequent molecules of methanol to a 1:2 solvate does not cause significant changes in the corresponding HBD distribution. The most dramatic changes are observed when the first two solvent molecules are added.

Considering water as another H-bonding solvent containing multiple H-bonding centers, MD simulations show that the population of different hydrogen-bonded

Table 2-6 Molecular dynamics results: the maxima of main peaks in the HBD distributions and the corresponding *fwhm* values; The equilibrium fractions (in percent) of the 1:1 cyclic doubly hydrogen-bonded complexes (see text for details) (Reproduced from [83] with permission from *Journal of Physical Chemistry A*. Copyright © 2000 American Chemical Society)

	Peak maximum [Å] ^a		fwhm [Å]		Equilibrium fraction cutoff [Å]	
	N···H-O	N-H···O	N···H-O	N-H···O	2.5	2.2
PQ + 1 MeOH	2.02	1.76	0.48	0.26	88	69
PQ + 2 MeOH	2.02	1.76	1.00	0.26	39	26
	2.02	3.58	0.44	0.54		
PQ in bulk MeOH	2.02	1.76	1.00	0.26	35	24
	2.15	4.49	0.56	1.22		
PQ + 1 H ₂ O	1.89	1.89	0.44	0.34	89	70
PQ + 2 H ₂ O	2.02	1.89	1.00	0.40	42	26
	2.15	3.71	0.52	0.54		
PQ in bulk H ₂ O	2.02	4.10	0.66	1.30	10	5
	3.19	2.02	1.10	0.40		
PyIn-2 + 1 MeOH	2.02	1.89	0.50	0.42	72	50
PyIn-2 + 2 MeOH	2.15	3.71	0.54	0.52	26	15
	2.54	1.89	1.02	0.30		
PyIn-2 in bulk MeOH	2.15 (a) ^b	1.76	0.58	0.36	15	9
	2.02 (b)	3.45	0.60	0.90		
	3.06 (c)	1.89	0.80	0.34		
PyIn-2 + 1 H ₂ O	1.89	2.02	0.58	0.36	74	47
PyIn-2 + 2 H ₂ O	1.89	2.02	0.44	0.40	31	19
	2.02	3.32	0.42	0.70		
PyIn-2 in bulk H ₂ O	2.15	1.89	0.52	0.32	5	3
	2.02	3.84	0.52	1.10		
	3.32	2.02	0.86	0.56		
7AI + 1 MeOH	2.28	1.89	1.28	0.36	37	13
7AI + 2 MeOH	1.89	3.45	0.34	0.50	1	0.1
	3.19	1.89	0.56	0.24		
7AI in bulk MeOH	1.89	5.14	0.30	0.86	0.9	0.1
	3.84	1.76	0.92	0.26		
7AI + 1 H ₂ O	2.15	2.15	0.60	0.68	35	11
7AI + 2 H ₂ O	1.89	3.45	0.26	0.46	0.1	0.01
	3.19	1.89	0.48	0.28		
7AI in bulk H ₂ O	1.89	4.49	0.30	1.00	0.01	—
	3.97	1.89	0.98	0.34		

^aAccuracy: ± 0.07 Å

^bCompare with Fig 2-9

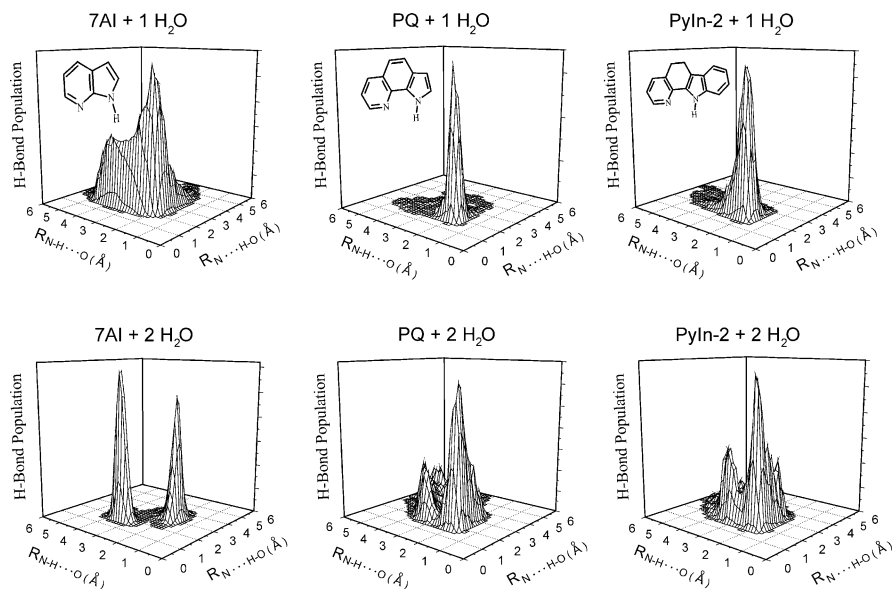


Figure 2-8. The HBD distributions for 7AI, PQ and PyIn-2 simulated for *n*-hexane in the presence of one and two molecules of water [83]

species and their structure are found to be in many aspects very similar to those obtained from the MD simulations in the presence of methanol. In the case of PQ and PyIn-2 with 1:1 and 1:2 solute:water stoichiometries, the cyclic, doubly hydrogen-bonded complex is present most of the time, as seen in Figure 2-8. Significant changes are observed for 7AI-(H₂O)₁, in which a considerable broadening of the HBD distribution is observed. The H-bonding intensity along the N-H···O coordinate is broadened and, at the same time, the corresponding distance along the N···H-O bond is shortened. In the case of 7AI-(H₂O)₂, similarly to 7AI-(MeOH)₂, most of the time the cyclic, triple hydrogen-bonded chain structure is found. Therefore, the MD simulations for the dilute solution with alcohol and water show that the topology of the H-bonding centers in PQ and PyIn-2 strongly favors the formation of the 1:1 cyclic hydrogen-bonded structure, even if the second solvent molecule is present in solution. 7AI also forms the cyclic, weakly hydrogen-bonded complex with protic solvent at 1:1 stoichiometry. However, in contrast to the behavior of PQ and PyIn-2, another, cyclic, 1:2 triply hydrogen-bonded structure is favored when more than one solvent molecule is available.

2.4.2. Hydrogen-Bonding Dynamics in Bulk Solvents

The MD simulations of the hydrogen bonding behavior of 7AI, PQ and PyIn-2 in bulk water and methanol show the increase of the probability of solute-solvent

hydrogen bonding in a long-distance region of HBD distribution, which is consistent with the formation of additional solvation shells around the solute. The corresponding intensity in the HBD graphs was cut off in order to improve the visualization of the hydrogen bonding distribution in the first solvation shell, as shown in Figure 2-9. The hydrogen bonding distribution for 7AI in bulk methanol shows the presence of two strong peaks. The comparison of peak positions and their breadth, seen as *fwhm* values in Table 2-6, with those observed in 7AI-(MeOH)₁ and 7AI-(MeOH)₂ demonstrates a significant peak broadening and shifts of the maximum of both peaks towards a long-range distance region compared to the case of the complexes in the dilute *n*-hexane solution (Figure 2-7). By tracing the hydrogen-bonding dynamics around 7AI in bulk methanol, it was shown that the two peaks correspond rather to a hydrogen-bonded complex in which 7AI is simultaneously hydrogen-bonded by its both, donor and acceptor atoms, with two molecules of methanol [83]. These methanol molecules are involved in independent hydrogen-bonding interactions with other molecules from the surrounding bulk methanol environment rather than with each other. It was also observed that during MD simulations these methanol molecules are being periodically exchanged by methanol molecules from the bulk. Therefore, the triple 1:2 hydrogen-bonded complex of 7AI with two methanol molecules, observed in the case of 7AI-(MeOH)₂, is strongly disfavored in bulk solution. What is most interesting, the equilibrium fraction of the 1:1 cyclic, doubly hydrogen-bonded complex was also found to decrease dramatically, so that its population is estimated to be smaller than 1%, as seen in Table 2-6.

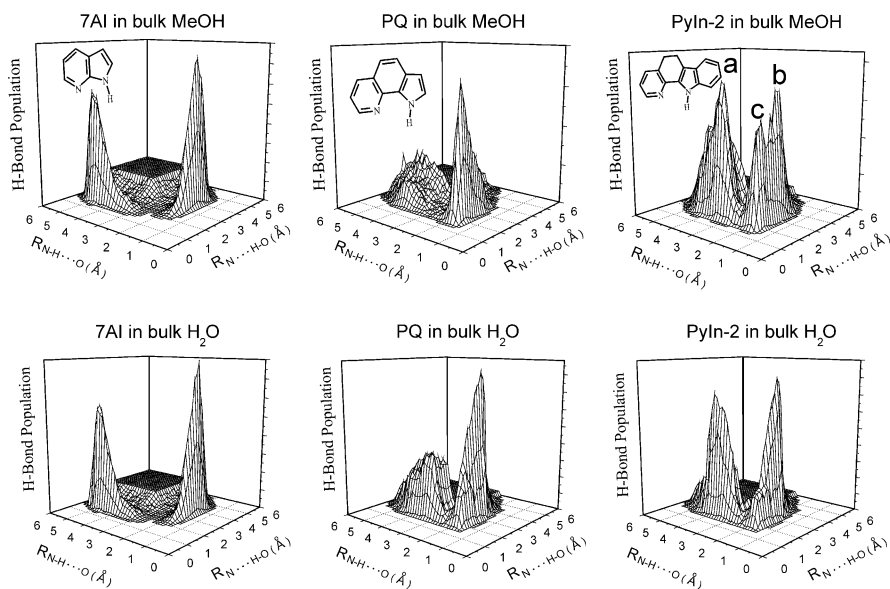


Figure 2-9. The HBD distributions for 7AI, PQ and PyIn-2 simulated for bulk methanol and for water solution [83]

The HBD distributions for PQ and PyIn-2 in bulk methanol and water are presented in Figure 2-9. The analysis of these distributions has shown that, despite of an extensive hydrogen-bonding nature of the bulk solvents, the significant equilibrium population of the 1:1 cyclic, double hydrogen-bonded species of PQ and PyIn-2 is still present (Table 2-6). In the case of PyIn-2, the three peaks (a, b and c in Figure 2-9, top-left) correspond to three differently hydrogen-bonded solvates, among which the peaks *a* and *b* can be assigned to the non-cyclic single hydrogen-bonded complexes, as schematically shown in Figure 2-6b for PQ, whereas the peak *c* is related to the 1:1 cyclic, double hydrogen-bonded species.

2.5. HYDROGEN-BONDING-INDUCED AND EXCITED-STATE PHENOMENA IN BIFUNCTIONAL DONOR-ACCEPTOR MOLECULES

Fluorescence spectra of hydrogen-bond bifunctional compounds such as PQ, DPC and PC are characterized by a single emission band in nonpolar (*n*-hexane) and polar aprotic (acetonitrile) solvents. Fluorescence quantum yields of these compounds have been reported to be quite high, 0.15–0.25 [8, 10, 55]. In alcohol and water solutions, the fluorescence quantum yield becomes very weak. The most interesting feature is the observation of dual fluorescence in the protic solvents [8–12, 55]. In addition to the first “normal” fluorescence band, referred to as F_1 , a second, long-wavelength band, F_2 , appears. The spectral position of F_1 is similar to that of the emission typically observed in polar aprotic solvents. The long-wavelength band F_2 , observed in protic media only, has been attributed to the fluorescent product of double proton tautomerization occurring in a photoexcited cyclically hydrogen-bonded complex of bifunctional azaaromatic compounds with protic solvent molecules [8–10]. The electron density redistribution occurring from the pyrrole to quinoline moieties upon excitation has been proposed to be the driving force for the excited-state tautomerization. PQ reveals an increase of the excited-state pK_a of the nitrogen atom in the acceptor quinoline moiety and a decrease of the corresponding pK_a of the donor NH group: $\Delta pK_a(N) = 9.6$ and $\Delta pK_a(NH) = -6.0$, respectively [55]. Such an acid–base excited-state behavior has been corroborated by the TDDFT calculations, which have shown a significant electron density redistribution from the donor to the acceptor part of PQ (Section 2.2). In addition to steady-state fluorescence studies, subpicosecond time-resolved fluorescence transient measurements carried out for PQ and PC have shown that the F_1 band contains two fast decay components with time constants of $\tau_1 = 0.6$ –0.9 ps and $\tau_2 = 6$ –11 ps, and a slower decay component, τ_3 , characterized by a time constant between 50 and 150 ps, depending on the properties of the alcohol [11]. The F_2 band has also revealed a fast biexponential rise occurring at the same rate as the fast initial decay of the emission band F_1 . It is interesting that no rise time corresponding to the slow decay of F_1 has been detected. Therefore, the time-resolved fluorescence experiments have provided convincing evidence that the F_1

and F_2 bands are emitted by different fluorescent species. The fast time decay components observed for F_1 and in the rise of F_2 have been attributed to the presence of cyclic hydrogen-bonded complexes of PQ with solvent molecules that are able to undergo solvent-assisted proton transfer. The longer decay component τ_3 of F_1 has been assigned to solute-solvent hydrogen-bonded complexes which are not involved the fast phototautomerization. An important finding is that the decay components τ_1 and τ_2 are only weakly dependent on temperature and viscosity [11]. This is in contrast to a strong temperature dependence of the slow component τ_3 . It has been concluded that cyclic, hydrogen-bonded complexes of the heteroazaaromatic species, with the structure appropriately prepared for a proton transfer reaction, are formed already in the ground state. Therefore, they do not require significant solvent relaxation around an excited bifunctional chromophore. This conclusion is consistent with the observation that the additional component τ_3 starts to appear in F_1 only when such a solvent relaxation process is activated in liquid solution at higher temperatures. It has also been proposed that since the slow component τ_3 has no corresponding counterpart in the rise of the fluorescence F_2 , the decay characterized by τ_3 should correspond to internal conversion from the photoexcited chromophore to its ground state [55]. The photophysics of different hydrogen-bonded species of bifunctional compounds with protic solvents is schematically summarized in Figure 2-10.

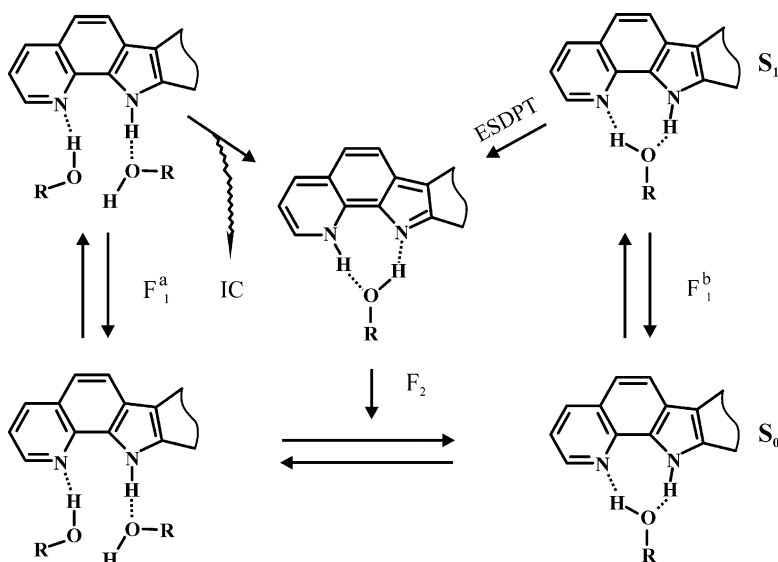


Figure 2-10. General scheme of the ground-state equilibrium between hydrogen-bonded complexes of bifunctional heteroazaaromatic molecules with protic solvents and photophysical processes occurring in hydrogen-bonded solvates [55]

The photophysics of bifunctional compounds composed of indole and pyridine moieties has recently been studied by Sobolewski and Domcke using *ab initio* electronic structure calculations [91–94]. It has been shown that, upon the electronic excitation, electron- and proton transfer processes are strongly correlated in these systems. It has been proposed that the photochemistry of such bifunctional compounds can be described in terms of the electron-driven-proton-transfer mechanism [92]. A common feature of such mechanism is the role of highly polar charge-transfer states, which induce the proton transfer reaction, leading in many cases to a conical intersection of the S_1 and S_0 state surfaces observed experimentally as ultrafast internal conversion.

2.6. INTERACTION OF HETEROAZAAROMATICS WITH LIPID MEMBRANES

Tryptophan, one of natural amino acids, is known to bind preferentially to the interfacial region of lipid membranes [95–97]. Therefore, membrane-bound tryptophan and other indole derivatives are found to be in easy contact with interfacial water. 7-azatryptophan and its analogs, closely related to 7-azaindole, have originally been designed as fluorescent probes with improved emission characteristics for studying solvation dynamics in biological systems [98]. The diversity of physical and chemical properties of these probes and, also, those that mimic natural amino acids and base-pair analogues, such as PQ derivatives, suggest that, due to their different hydrophobicities, binding modes of these probes with lipid membranes may differ significantly. To address this question, we used classical all-atom MD simulations to study interactions and favorable locations of several heteroazaaromatic compounds, such as 7AI, PQ and PC inside a lipid membrane [99].

A membrane is modeled using a phospholipid bilayer composed of 128 dipalmitoylphosphatidylcholine (DPPC) lipids surrounded by 4310 water molecules. In such a system, a lipid-to-water ratio is about 1:33, so that the lipid bilayer is considered to be in the fully hydrated state [100]. In order to model a bilayer existing in a biologically relevant liquid crystalline phase the simulation is carried out at the temperature of 323 K. Figure 2-11 shows an example of the simulated system containing a hydrated DPPC bilayer with several molecules of PQ partitioned inside the hydrophobic core of the membrane. Although such a snapshot represents a single, instantaneous configuration of the system, averaging over many configurations and for a long period of MD runs allows one to obtain average density profiles for individual components of a bilayer [101], as well as a distribution profile of probe molecules diffusing freely across an MD box during simulations (Figure 2-11, right).

Interactions and binding modes of a series of heteroazaaromatic probes with a lipid membrane are modeled using classical MD simulations at the constant number of particles, constant pressure of 1 atm, and constant temperature, $T = 323$ K (NPT

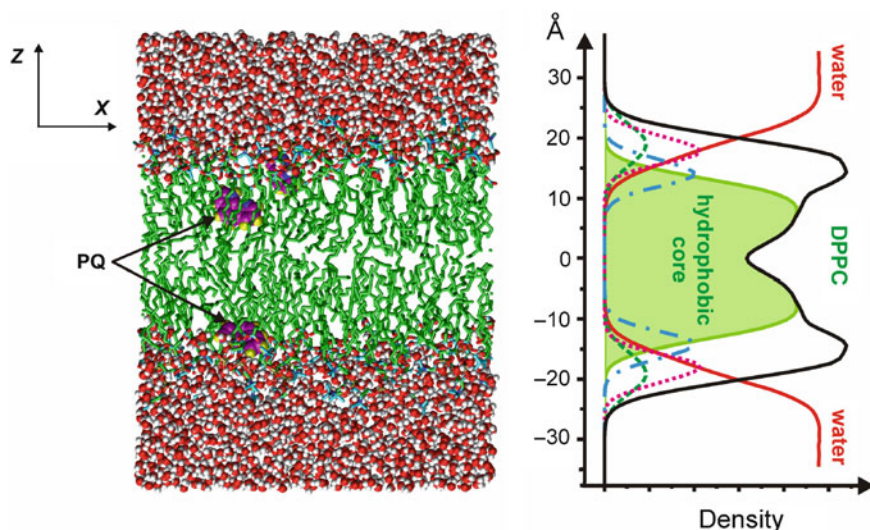


Figure 2-11. (Left panel) Snapshot of a hydrated DPPC bilayer after 50 ns of MD simulations. PQ molecules are drawn in vdW representation. (Right panel) Mass density profiles of different molecular components of a DPPC bilayer. The mass densities were obtained by averaging MD trajectories for the last 40 ns. Solid black and red lines show the densities of DPPC and water across the MD box. Other individual components of the bilayer are plotted as follows: acyl chains, showing a hydrophobic core of the bilayer, (solid light green line), choline (dashed green line), phosphate (dotted magenta line) and glycerol (dash-dotted blue line) moieties, respectively

ensemble). Statistical averaging is applied to accumulate a distribution profile of a probe between water solution, at biological pH (pH about 7), and a bilayer. The simulations are designed to reproduce the passive, thermally-driven diffusion of the probes in the simulation box. At the beginning of the simulation, eight molecules of each probe (7AI, PQ and PC) are added, in a random fashion, into the aqueous solution at the vicinity of the bilayer interface (four probes per each, top and bottom, leaflet of the bilayer). The initial MD configuration of a PQ/DPPC system containing eight PQ molecules at $t = 0$ ns is shown in Figure 2-12. The MD simulations demonstrate that, during the first 10 ns, the probe molecules tend to diffuse from the aqueous phase into the polar interfacial region of the DPPC bilayer. After 20 ns, all the probe molecules are found to be located preferentially at the bilayer interface, as shown in Figure 2-12 for the PQ/DPPC system at $t = 20$ ns. Further time evolution of membrane interactions of 7AI, PQ and PC with the bilayer shows a similar behavior for all the probes, so that when they reach the headgroup region of the membrane, their diffusion slows down significantly. At the end of the 50 ns simulation period, 7AI was found to be distributed broadly across the bilayer interface, whereas PQ and PC were located deeper inside the hydrocarbon core of the DPPC bilayer. A typical distribution of the PQ molecules at the end of the 50 ns MD run is shown in Figure 2-12.

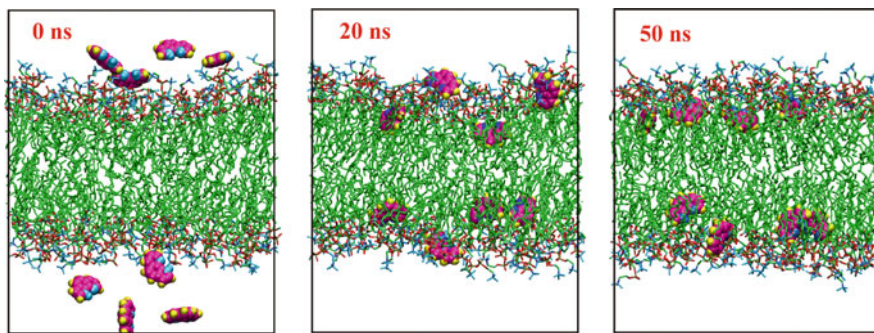


Figure 2-12. Snapshots of the MD boxes taken from the simulations of eight PQ molecules in the DPPC bilayer after $t = 0, 20$ and 50 ns of the NPT simulation. Water molecules are not shown for clarity. The PQ molecules are rendered with enlarged atomic van der Waals radii [99]

The quantitative evaluation of the distribution of 7AI, PQ and PC within the DPPC bilayer is represented by mass density profiles of different molecular components across the bilayer. Figure 2-13 shows the density distributions for choline, phosphate, as well as the glycerol backbone and acyl chains of the phospholipid molecules across the bilayer. The density of 7AI, PQ and PC molecules within the DPPC bilayer is also shown in Figure 2-13a–c. As can be seen, the three probes demonstrate a different localization behavior and different penetration depths in the DPPC bilayer. The density profiles also reveal a different number of the binding sites for these probes. 7AI is found to be distributed throughout the interfacial region to the hydrocarbon acyl chain core of the bilayer. The preferable localization of PC is much deeper inside the hydrocarbon region of the bilayer, below the glycerol moiety of lipids. In the case of PQ, two binding sites, located at two different depths inside the bilayer, can be identified; a major site is localized in the hydrocarbon core and a second, minor population is observed at the membrane interface (Figure 2-13b).

The results of decomposition analysis of the density profiles of the binding sites of the three probes are summarized in Table 2-7. Comparison of the site localization shows that the molecular shape and aromaticity of the probes play an important role in their localization in the lipid membrane. The favorable probe location is found to be determined by the hydrophobic effect. The three probes differ in the number of their aromatic rings, increasing in the following sequence: 7AI–PQ–PC. Therefore, the hydrophobic character of the probes also increases in the same order. The tendency to drive the aromatic hydrocarbon probe out of polar water results in their deep membrane localization inside the bilayer. As can be seen in Table 2-7, the depth of the probe localization in this sequence is gradually shifted from interfacially localized (sites B and C) to deeply inserted into the hydrocarbon acyl chain core of the bilayer (site A) (Table 2-7).

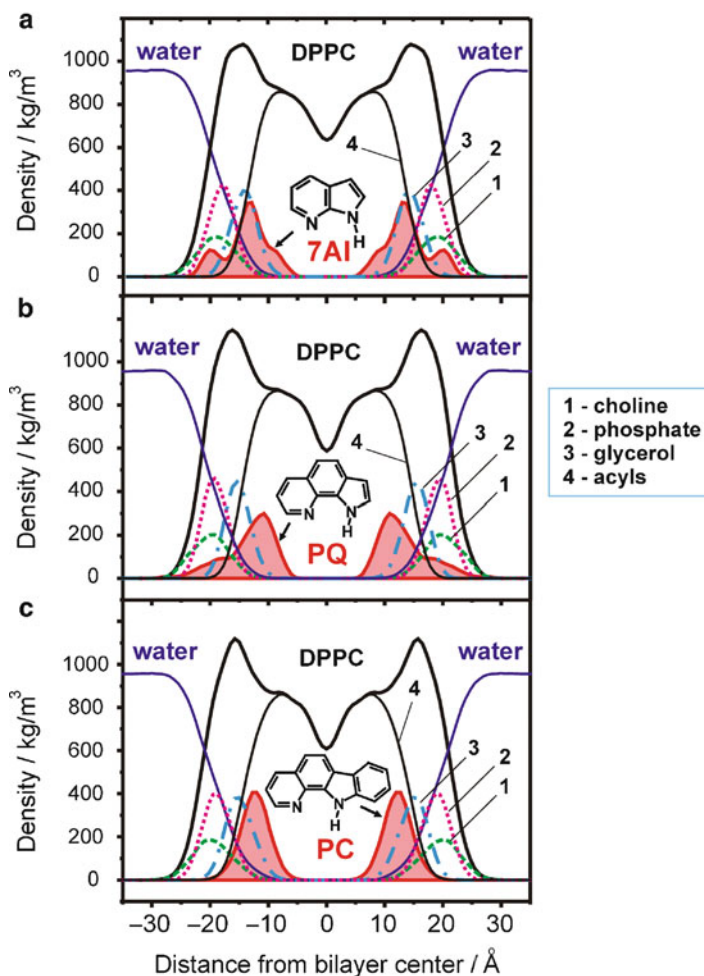


Figure 2-13. Mass density distribution profiles for individual components of the DPPC bilayer and for the total density distribution of eight molecules of 7AI (a), PQ (b) and PC (c). The DPPC components are: 1 – choline group; 2 – phosphate group; 3 – glycerol moiety; 4 – acyl chains. All the density profiles are plotted with respect to the center of the z-axis of the MD box [99]

2.6.1. Hydrogen-Bonding at the Membrane Interface

The three probes, 7AI, PQ, and PC, bind to the DPPC membrane in a different fashion. They also penetrate into the hydrocarbon region of the bilayer at different depths. As a result, hydrogen-bonding of these probes with water molecules and with polar headgroups of the bilayer may also differ significantly. Figure 2-14a shows the geometrical criteria for the existence of a hydrogen bond between a probe

Table 2-7 Summary of Gaussian decomposition analysis for probe-membrane binding sites [99] (Reproduced from [99] with permission from *Biophysical Chemistry*. Copyright © 2008 Elsevier)

Binding site	7AI			PQ			PC		
	P ^a (%)	Max ^b (Å)	Fwhm ^c (Å)	P (%)	Max (Å)	Fwhm (Å)	P (%)	Max (Å)	Fwhm (Å)
A	15	8.6	3.0	62	11.0	4.6	100	12.2	4.9
B	65	13.3	3.8	38	17.2	8.3	–	–	–
C	20	19.8	3.3	–	–	–	–	–	–

^aPopulation (P) of a binding site

^bMaximum of a Gaussian band

^cFull width at half maximum

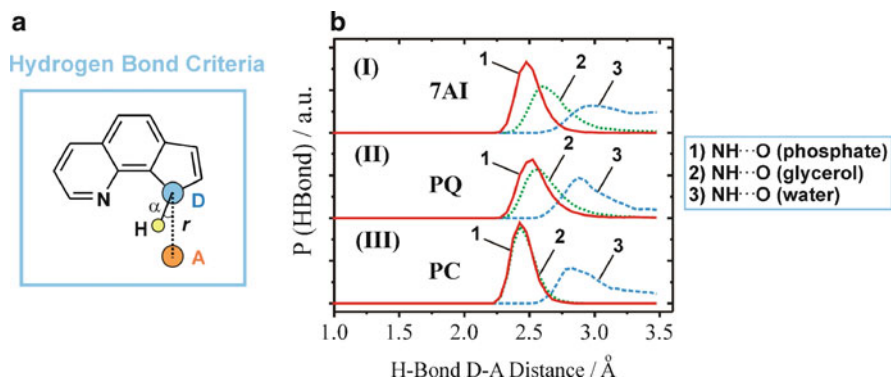


Figure 2-14. (a) Geometrical criteria ($r_{\text{HB}} \leq 3.5$ Å and $\alpha_{\text{HB}} \leq 30^\circ$) for hydrogen-bonding between a donor (D) and an acceptor (A) in PQ. (b) Distribution of hydrogen bond donor-acceptor distances for 7AI (I), PQ (II), and PC (III). The distance distribution between the donor (the imino nitrogen atom (NH) of the probe molecule) and the acceptor (oxygen atoms of a lipid phosphate group) is shown by a solid line (1); between the donor and oxygen atoms of a lipid glycerol moiety by a dotted line (2); between the donor and water oxygen atoms by a dashed line (3) [99]

molecule acting as a donor and the oxygen atoms of water or lipids as acceptors. A hydrogen bond between a donor and an acceptor is assumed to exist if the D-A distance (r_{HB}) and the angle (α_{HB}) fulfill the following criteria: $r_{\text{HB}} \leq 3.5$ Å and $\alpha_{\text{HB}} \leq 30^\circ$. The imino nitrogen atom of a probe was chosen as an H-bond donor and oxygen atoms of water, phosphate and glycerol groups served as H-bond acceptors.

To determine the nature of favorable hydrogen bonds formed between the probe and interfacial waters or the DPPC lipids, the relative frequency of the occurrence of each type of these H-bonds was estimated. The results of the hydrogen-bonding analysis are summarized in Table 2-8. As can be seen, the majority (~95%) of 7AI population is found to be hydrogen-bonded with either water or lipid molecules of the bilayer, whereas a significant fraction (about 24% and 33%) of PQ and PC, respectively, exists in a hydrogen-bond-free form. 7AI was found to be localized on the water/bilayer interface and, therefore, a large population of probe molecules

Table 2-8 Results of the analysis of hydrogen-bonding between the probe molecules and lipids and water (Reproduced from [99] with permission from *Biophysical Chemistry*. Copyright © 2008 Elsevier)

Hydrogen bond	7AI				PQ				PC			
	F ^a (%)	r _{HB} ^b (Å)	fwhm ^c (Å)	α _{HB} ^d (deg)	F ^a (%)	r _{HB} ^b (Å)	fwhm ^c (Å)	α _{HB} ^d (deg)	F ^a (%)	r _{HB} ^b (Å)	fwhm ^c (Å)	α _{HB} ^d (deg)
NH–water oxygen	44.4	2.98	0.58	11.5	26.8	2.88	0.37	12.0	22.8	2.83	0.42	14.0
NH–phosphate oxygen	39.5	2.49	0.19	5.5	21.8	2.52	0.22	8.5	14.3	2.42	0.17	6.5
NH–glycerol oxygen	10.9	2.60	0.27	6.5	27.3	2.57	0.26	9.0	29.4	2.44	0.16	8.5
no H-Bonds	5.2	–	–	–	24.1	–	–	–	33.5	–	–	–

^aRelative frequency (F) of the occurrence of hydrogen-bonding

^bDistribution peak of the H-bond donor–acceptor distance, see Figure 2-14 for details

^cFull width at half maximum of the H-bond donor–acceptor distance distribution

^dAverage deviation of the H-bond from linearity

exist in permanent contact with interfacial water, as also seen from the corresponding density profiles in Figure 2-13a. Therefore, the relative frequency of the occurrence of hydrogen-bonds between 7AI and water was estimated to be about 44% (Table 2-8). For comparison, in the case of PQ and PC, hydrogen-bonding with water is gradually decreased to $\sim 27\%$ and $\sim 23\%$, respectively, in agreement with the deeper located major binding sites of these probes inside the hydrophobic, water-free region of the bilayer. The distribution of the hydrogen bonds distances is shown in Figure 2-14b and Table 2-8. The H-bond distance and angle distributions demonstrate that all the three probes, 7AI, PQ and PC, form relatively strong hydrogen bonds with the oxygen atoms of the phosphate group of the lipids. However, this effect may not be decisive in favoring the probe localization in the bilayer, because significant populations of PQ and PC are still found to exist as hydrogen-bond-free, indicating that the favorable binding of these probes into the hydrocarbon core of the bilayer is not completely driven by hydrogen-bonding.

There is a significant overlap between the density distribution profiles of the probe and water molecules, penetrating deeply into the headgroup region of the bilayer, as seen in Figure 2-13a–c. The above-presented hydrogen-bonding analysis described the statistically averaged hydrogen-bonding interactions accumulated over a long MD simulation period of 40 ns. We also evaluated a partial radial distribution function $g(R)$ as a complementary tool for the H-bonding analysis. The $g(R)$ function was calculated between the imino NH hydrogen atom of the probe, assumed to be an H-bond donor, and the oxygen atoms of the lipid molecules (Figure 2-15). The analysis shows that, for all the three probes, the first peak of $g(R)$ is observed between the NH hydrogen atom of the probe and the oxygen atoms of either the phosphate or glycerol groups of the DPPC lipids. The $g(R)$ peak for 7AI, PQ and PC are observed at distances of 1.5–1.6 Å, respectively. This distance range corresponds to values of hydrogen-bond lengths evaluated by MD simulations for H-bonded water complexes of these compounds in bulk solution [83, 99].

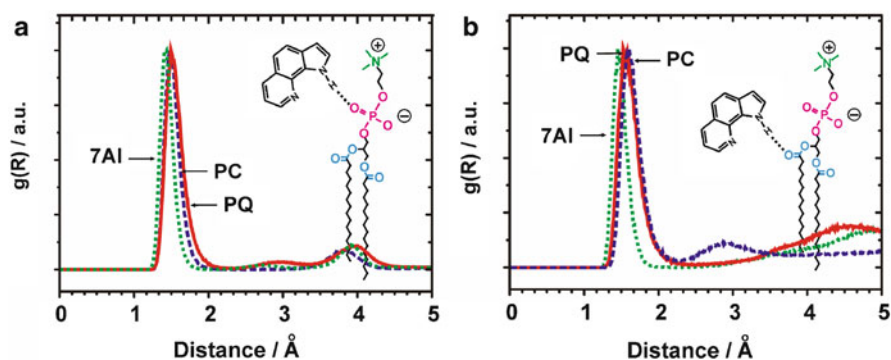


Figure 2-15. Radial pair distribution functions $g(R)$ of the N-H hydrogen atom of PQ (solid line), PC (dashed line) and 7AI (dotted line) around the oxygen atoms of the phosphate (a) and glycerol (b) groups of the DPPC lipids. The corresponding hydrogen-bonding between the probe and lipid molecules is schematically shown for PQ [99]

2.7. PROBING THE ACID–BASE EQUILIBRIUM AT THE MEMBRANE INTERFACE

Excited-state proton transfer (ESPT) has been reported for 2-(2'-pyridyl)benzimidazole (2PBI) in aqueous solutions at acidic pH [102]. It has been observed that the reaction occurs predominantly in the cationic form, 2PBI⁺, in which the second benzimidazole nitrogen atom is protonated, as shown schematically in Figure 2-16a. It has also been proposed that the ESPT in 2PBI is assisted by hydrogen-bonding with water molecules. Therefore, according to refs [103, 104], one of the requirements for ESPT in 2PBI to occur is the formation of a cyclic, hydrogen-bonded complex with protic partner molecules (Figure 2-16b).

The solvent-mediated ESPT in such systems is often characterized by high sensitivity to the properties of a surrounding medium. It has been recently shown that ESPT in hydrogen-bonded complexes of 2PBI is selectively enhanced at a micelle-water interface [103]. One of possible reasons for this phenomenon is that the cationic form 2PBI⁺ could be stabilized by favorable electrostatic interactions with the charged surface of micellar systems [104]. This effect could have important implications in fluorescence sensing of structure and dynamics of the interface of cell membranes. Therefore, the knowledge of interactions and binding modes of 2PBI derivatives with lipid membranes could allow understanding of possible mechanisms of the modulation of an ESPT reaction at a heterogeneous membrane environment.

In order to understand interactions and preferable binding modes of 2-(2'-pyridyl)benzimidazole with a model membrane we applied a molecular dynamics approach

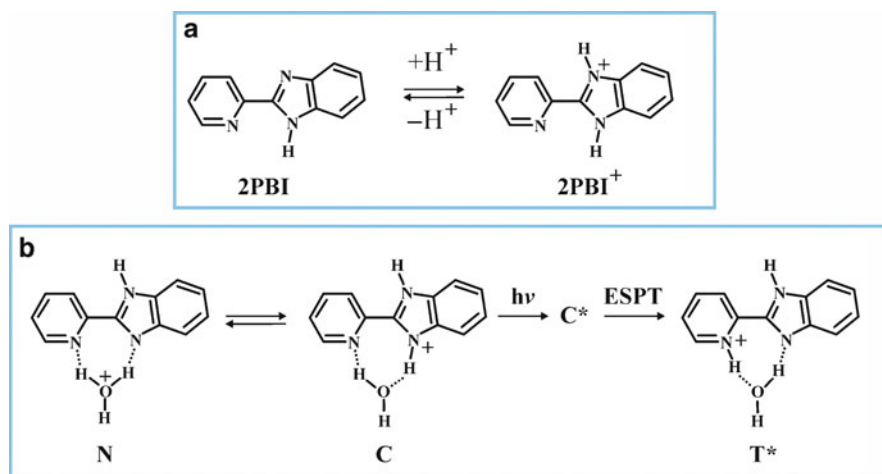


Figure 2-16. (a) Scheme of acid–base equilibrium in 2-(2'-pyridyl)benzimidazole. (b) Mechanism of the photoinduced proton transfer in a cyclic, hydrogen-bonded complex of a cationic form of 2PBI with water

described in Section 2.6. To model an acid–base equilibrium in solution and at a membrane interface, both the neutral (2PBI) and cationic (2PBI⁺) forms were simultaneously present in MD simulations. Two neutral and two cationic species were initially placed in the water region near the top and the bottom leaflets of a DPPC bilayer, so that a total number of eight solute molecules were sampled in MD simulations. The initial configuration of the simulated system at $t = 0$ ns is shown in Figure 2-17. Simultaneous MD sampling of the membrane interaction of the two different, neutral and cationic, forms of 2PBI under the same simulation conditions allows us to understand in more detail preferable distribution of each of these forms between the aqueous solution and the lipid bilayer. Different polarities of 2PBI and 2PBI⁺ imply that these two species will partition into different, apolar and polar, regions of a bilayer [105], where concentrations of water molecules are different [106, 107]. Therefore, the formation of hydrogen-bonded complexes of 2PBI and 2PBI⁺ with water may be modulated by localization of these species in different regions of a bilayer.

In the applied MD approach, both 2PBI and 2PBI⁺ species were allowed to diffuse freely between the aqueous solution and the lipid bilayer, so that sampling over a long MD simulation period can provide the overall probability to find each of

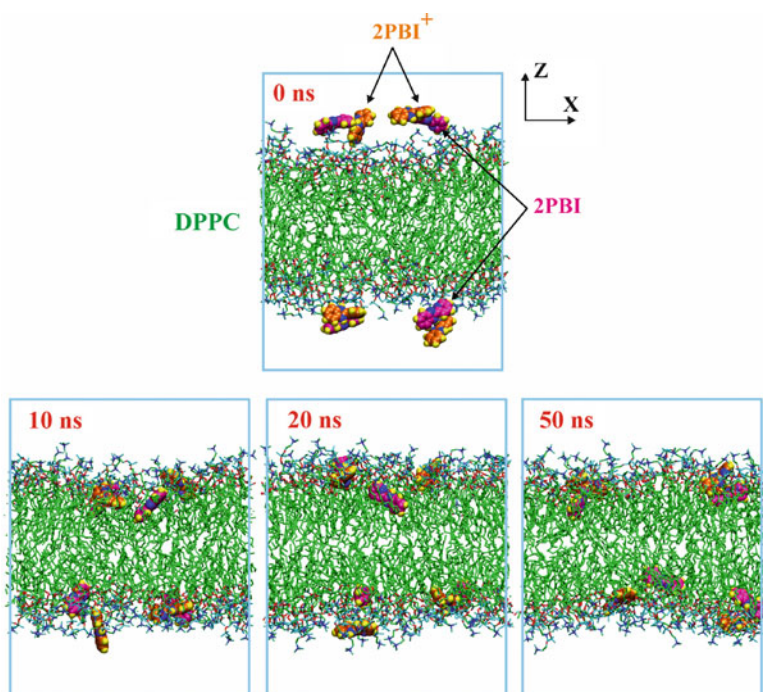


Figure 2-17. MD simulations of the interactions of neutral (2PBI) and cationic (2PBI⁺) forms of 2-(2'-pyridyl)benzimidazole with a DPPC bilayer. Snapshots are shown for an initial MD configuration ($t = 0$ ns) and after 10, 20 and 50 ns. Water molecules are not shown

these species across bulk water/interface/membrane core regions. The time evolution of the distribution of 2BPI and 2BPI⁺ between bulk solution and the DPPC bilayer is illustrated in Figure 2-17. As can be seen from the first 10 ns of the MD sampling, both the neutral and cationic forms are moving towards the bilayer interface. At longer simulation times of 20–50 ns, further redistribution occurs between the species located at the membrane interface and the solute molecules deeply-inserted into a hydrocarbon core of DPPC.

The localization probability of the probe molecules can be described by their mass density profile acquired across the bilayer [99,101]. The mass densities of neutral 2BPI and cationic 2BPI⁺ were therefore evaluated along the bilayer axis z , as defined in Figure 2-17. Figure 2-18 shows the time evolution of the mass densities which are averaged starting from $t = 0$ ns and ending at time intervals of 2, 10, 20 and 50 ns, respectively. As can be noticed, at these time intervals the major peak of the mass density of the polar cationic form 2BPI⁺ is always found to be located in more polar interfacial regions of the bilayer compared to that of the neutral form 2BPI. At $t = 2$ ns 2BPI⁺ is preferably located at 22.1 Å from the bilayer center (Figure 2-18). A second binding site for 2BPI⁺ is also observed at 17.4 Å. Both these populations of 2BPI⁺ can be assigned to interfacial binding sites. In the same time interval of 2 ns, 2BPI is also characterized by a dual peak distribution with the maxima located at 18.7 and 22.7 Å, respectively. The major population of 2BPI is, however, found to be shifted towards the hydrophobic region of the bilayer. The time evolution of the densities shows that, at longer time intervals of 10–20 ns, the major population of 2BPI⁺ becomes preferably concentrated at the binding site located at 16.5–17.4 Å, whereas the population originally observed at 22.1 Å gradually decreases and its peak position is shifted to 20.7 Å (Figure 2-18). A similar population redistribution occurs between two originally observed binding sites of 2BPI. The population of 2BPI, which is observed at 22.7 Å at $t = 2$ ns, has a very small contribution to the overall population evaluated after 20 ns of the MD sampling. At the same time, the peak of the major population of 2BPI is localized at 15.0–15.4 Å, respectively. At $t = 50$ ns, 2BPI⁺ can be characterized by the mass density distribution with one, well-defined, population located at 17.0 Å. At the same time, 2BPI is preferably located at 13.7 Å, so that it is more deeply buried into the bilayer compared to the polar cationic form 2BPI⁺.

The density distributions of 2BPI and 2BPI⁺, as well as those of the DPPC bilayer and water, averaged over all 50 ns of the MD sampling period are presented in Figure 2-19. As can be seen, the preferable localizations of 2BPI and 2BPI⁺ are driven by different factors. The major population of neutral and, therefore, more hydrophobic 2BPI is located inside the hydrophobic core of the bilayer formed by its acyl chains. In contrast, 2BPI⁺ is found to be strongly localized at the interface. The depth of its distribution into the bilayer correlates and coincides well with the depth of water penetration into the bilayer, as is clearly seen in Figure 2-19. Therefore, polar cationic 2BPI⁺ prefers to be located in the region of the bilayer with high concentration of water molecules.

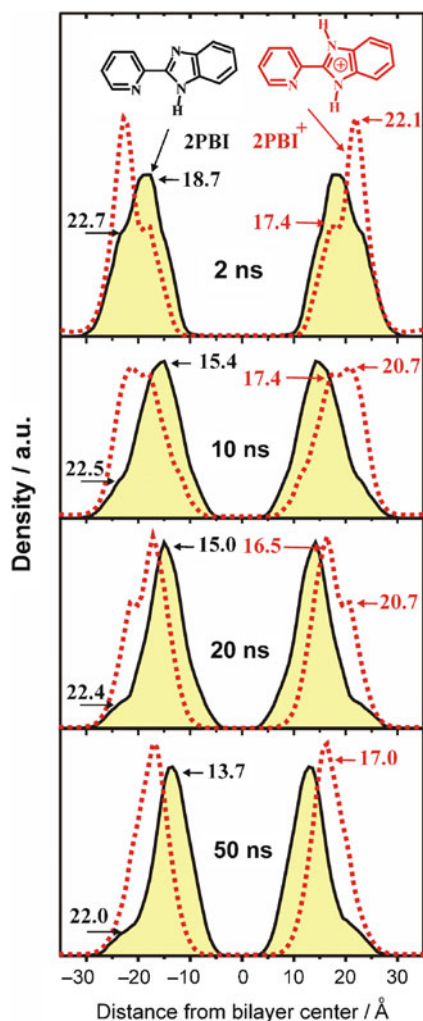


Figure 2-18. Time evolution of the mass density of neutral 2PBI and the cationic form 2PBI⁺ calculated across an MD simulation box along the z axis of the DPPC bilayer (see Figure 2-17 for details). Peak positions of major binding sites are shown in angstroms

Owing to distinct binding localizations and the different hydrogen-bonding-dependent fluorescence behavior of neutral and cationic forms 2PBI and 2PBI⁺ in the lipid bilayer, it is possible to apply this compound for studying the properties of biological water of the bilayer interface. Recently, it has been shown, by measuring time-resolved fluorescence spectra and kinetics, that the excited-state proton transfer dynamics of 7AI in water nanopools of reverse micelles is slowed down compared to bulk water solution [108]. It has been concluded that, because 7AI is preferably located in the bound-water regions of reverse micelles, higher free

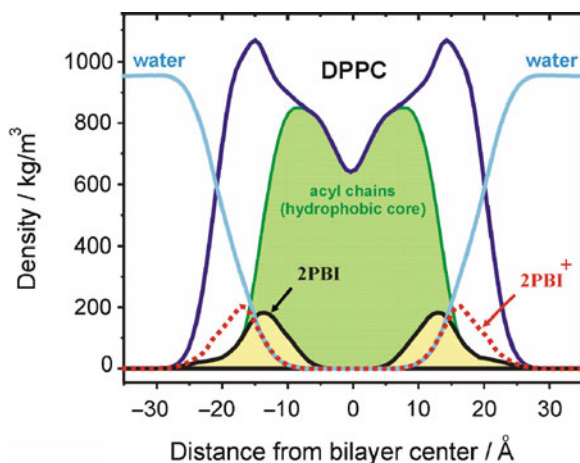


Figure 2-19. Average density distributions of the DPPC bilayer, water and probe molecules (2PBI and 2PBI⁺) along the z axis of the simulation box (see Figure 2-17 for details). The density averaging was performed over 50 ns of the MD simulation

energy is required for solvation of reactive, cyclically hydrogen-bonded species of 7AI in confined water environment. The cationic form 2BPI⁺ is able to form hydrogen-bonded solvates with interfacial water molecules in which its excited-state behavior is altered by proton transfer reaction. Therefore, the fluorescence of 2BPI⁺ bound to a lipid membrane may be used as a tool for better understanding of water dynamics in structured biological environments.

2.8. CONCLUSIONS

We have presented an overview of the results of computational and experimental works concerning structures, hydrogen-bonding dynamics and excited-state properties of a series of bifunctional hydrogen-bond donor–acceptor heteroazaaromatic compounds of biological importance. The common thread in the photophysics of these compounds is the important role of cyclic hydrogen-bonded solvates formed with protic partner molecules. The cyclic hydrogen-bonding with external partners, connecting proton donor and acceptor parts of a heteroazaaromatic molecule, enables multiple proton transfer phototautomerism, which is not possible in the case of an isolated, hydrogen-bond-free chromophore. Using *ab initio* and DFT computational approaches we have provided physical insights and qualitative interpretation of the role of hydrogen-bonding and cluster size effects for the photophysics of jet-isolated PQ clusters [84, 85]. The ultrashort excited state lifetime observed for the cyclic, double hydrogen-bonded complex PQ–(MeOH)₁ has been found to be due to the rapid double proton transfer reaction followed by nonradiative relaxation. In the larger size, jet-cooled, clusters of PQ with methanol, the cyclic, however, less

favorable hydrogen bonding blocks the fast proton transfer tautomerization. The structure of hydrogen-bonded solvates and preferable hydrogen-bonding modes of bifunctional compounds in bulk solvents have been further explored by classical molecular dynamics. We have found, using several lines of evidence based on both experimental results and quantum chemical/molecular dynamics simulations, that the structural topology of proton donor and acceptor parts of bifunctional solute molecules composed of a pyrroloquinoline-like moiety favors the formation of the cyclic, 1:1 double hydrogen-bonded solvates even in bulk hydroxylic solvents. Such hydrogen-bonding behavior of PQ and related compounds is quite different from that of another family of bifunctional donor–acceptor molecules based on 7AI and 1-azacarbazole. The latter compounds appear to form hydrogen-bonded complexes with the 1:2 solute-solvent stoichiometry [62, 78]. These results show that a mere shifting of the donor and acceptor groups by just one bond away from each other may lead to dramatic structural effects which, in turn, control the photophysics and photochemistry of hydrogen-bonded complexes.

The possible effect of microsolvation on the excited-state proton transfer and fluorescence quenching of bifunctional compounds in a heterogeneous environment of a lipid bilayer has also been discussed. The MD simulations have shown that the depth of the localization of the heteroazaaromatics probes inside a lipid membrane may be tuned by small structural modification of a parent probe molecule [99]. It appears that the bifunctional chromophores can be used as probes of local polarity, viscosity, and hydrophilicity, as well as indicators of specific hydrogen-bonding topologies [13].

Finally, it should be noted that the MD methodologies similar to those presented above have been used to explain other types of environment-specific phenomena: (i) solvent-induced conformational changes [1, 109]; (ii) rare gas matrix deposition, origin of site-structure and its energetics [110–113].

ACKNOWLEDGEMENTS

JW acknowledges support by the grant N N204 3329 33 from the Polish Ministry of Science and Higher Education. The experiments referred to in this work were based on a long-time collaboration with the groups of Prof. R.P. Thummel (University of Houston) and Prof. B. Brutschy (University of Frankfurt).

REFERENCES

1. Waluk J (2003) *Acc Chem Res* 36:832–838
2. Chou PT (2001) *J Chin Chem Soc* 48:651–682
3. Nosenko E, Wiosna-Sałyga G, Kunitski M, Petkova I, Singh A, Buma WJ, Thummel RP, Brutschy B, Waluk J (2008) *Angew Chem Int Ed Engl* 47:6037–6040
4. Kijak M, Nosenko E, Singh A, Thummel RP, Waluk J (2007) *J Am Chem Soc* 129:2738–2739
5. Wiosna-Sałyga G, Dobkowski J, Mudadu MS, Sazanovich I, Thummel RP, Waluk J (2006) *Chem Phys Lett* 423:288–292

6. Kijak M, Zielińska A, Chamchoumis C, Herbich J, Thummel RP, Waluk J (2004) *Chem Phys Lett* 400:279–285
7. Wiosna G, Petkova I, Mudadu MS, Thummel RP, Waluk J (2004) *Chem Phys Lett* 400:379–383
8. Herbich J, Dobkowski J, Thummel RP, Henge V, Waluk J (1997) *J Phys Chem A* 101:5839–5845
9. Kyrchenko A, Herbich J, Izydorzak M, Gil M, Dobkowski J, Wu FY, Thummel RP, Waluk J (1999) *Isr J Chem* 39:309–318
10. del Valle JC, Dominguez E, Kasha M (1999) *J Phys Chem A* 103:2467–2475
11. Marks D, Zhang H, Borowicz P, Waluk J, Glasbeek M (2000) *J Phys Chem A* 104:7167–7175
12. Kijak M, Zielińska A, Thummel RP, Herbich J, Waluk J (2002) *Chem Phys Lett* 366:329–335
13. Herbich J, Kijak M, Luboradzki R, Gil M, Zielińska A, Hu YZ, Thummel RP, Waluk J (2002) *J Photochem Photobiol: A Chem* 154:61–68
14. Taylor CL, El-Bayoumi MA, Kasha M (1969) *Proc Natl Acad Sci USA* 63:253–260
15. Douhal A, Kim SK, Zewail AH (1995) *Nature* 378:260–263
16. Folmer DE, Poth L, Wisniewski ES, Castleman AW Jr (1998) *Chem Phys Lett* 278:1–7
17. Takeuchi S, Tahara T (1998) *J Phys Chem A* 102:7740–7753
18. Takeuchi S, Tahara T (2001) *Chem Phys Lett* 347:108–114
19. Fiebig T, Chachisvilis M, Manger M, Zewail AH, Douhal A, Garcia-Ochoa I, de La Hoz AA (1999) *J Phys Chem A* 103:7419–7431
20. Folmer DE, Wisniewski ES, Castleman AW Jr (2000) *Chem Phys Lett* 318:637–643
21. Catalán J, del Valle JC, Kasha M (1999) *Proc Natl Acad Sci USA* 96:8338–8343
22. Catalán J, Pérez P, del Valle JC, de Paz JLG, Kasha M (2002) *Proc Natl Acad Sci USA* 99:5793–5798
23. Takeuchi S, Tahara T (2007) *Proc Natl Acad Sci USA* 104:5285–5290
24. Kwon OH, Zewail AH (2007) *Proc Natl Acad Sci USA* 104:8703–8708
25. Catalán J (2008) *Proc Natl Acad Sci USA* 105:E78
26. Kwon OH, Zewail AH (2008) *Proc Natl Acad Sci USA* 105:E79
27. Sekiya H, Sakota K (2008) *J Photochem Photobiol: C Photochem Rev* 9:81–91
28. Fang WH (1998) *J Am Chem Soc* 120:7568–7576
29. Kohtani S, Tagami A, Nakagaki R (2000) *Chem Phys Lett* 316:88–93
30. Matsumoto Y, Ebata T, Mikami N (2002) *J Phys Chem A* 106:5591–5599
31. Meuwly M, Bach A, Leutwyler S (2001) *J Am Chem Soc* 123:11446–11453
32. Coussan S, Meuwly M, Leutwyler S (2001) *J Chem Phys* 114:3524–3534
33. Tanner C, Manca C, Leutwyler S (2003) *Science* 302:1736–1739
34. Bach A, Tanner C, Manca C, Frey HM, Leutwyler S (2003) *J Chem Phys* 119:5933–5942
35. Manca C, Tanner C, Coussan S, Bach A, Leutwyler S (2004) *J Chem Phys* 121:2578–2590
36. Tanner C, Manca C, Leutwyler S (2005) *J Chem Phys* 122:204326/1–204326/11
37. Fernández-Ramos A, Martínez-Núñez E, Vázquez SA, Ríos MA, Estévez CM, Merchán M, Serrano-Andrés L (2007) *J Phys Chem A* 111:5907–5912
38. Mehata MS (2007) *Chem Phys Lett* 436:357–361
39. Mehata MS (2008) *J Phys Chem B* 112:8383–8386
40. Zimmer M (2002) *Chem Rev* 102:759–781
41. Vendrell O, Gelabert R, Moreno M, Lluch JM (2008) *J Chem Theory Comp* 4:1138–1150
42. Pakhomov AA, Martynov VI (2008) *Chem Biol* 15:755–764
43. Vendrell O, Gelabert R, Moreno M, Lluch JM (2008) *J Phys Chem B* 112:5500–5511
44. Vendrell O, Gelabert R, Moreno M, Lluch JM (2008) *J Phys Chem B* 112:13443–13452
45. Kandori H (2000) *Biochim Biophys Acta* 118:177–191
46. Sato Y, Hata M, Neya S, Hoshino T (2006) *J Phys Chem B* 110:22084–22812
47. Bondar AN, Baudry J, Suhai S, Fischer F, Smith JC (2008) *J Phys Chem B* 112:14729–14741

48. Serrano-Andrés L, Roos BO (1996) *J Am Chem Soc* 118:185–195
49. Sobolewski AL, Domcke W (1999) *Chem Phys Lett* 315:293–298
50. Kyrychenko A, Waluk J (2006) *J Phys Chem A* 110:11958–11967
51. Parac M, Grimme S (2002) *J Phys Chem A* 106:6844–6850
52. Hättig C, Köhn A (2002) *J Chem Phys* 117:6939–6951
53. Nosenko Y, Kunitski M, Riehn C, Thummel RP, Kyrychenko A, Herbich J, Waluk J, Brutschy B (2008) *J Phys Chem A* 112:1150–1156
54. Furche C, Ahlrichs R (2002) *J Chem Phys* 117:7433–7447
55. Kyrychenko A, Herbich J, Izydorzak M, Wu F, Thummel RP, Waluk J (1999) *J Am Chem Soc* 121:11179–11188
56. Kornyshev AA, Kuznetsov AM, Spohr E, Ulstrup J (2003) *J Phys Chem B* 107:3351–3366
57. Agmon N (2005) *J Phys Chem A* 109:13–35
58. Lapid H, Agmon N, Petersen MK, Voth GA (2005) *J Chem Phys* 122:014506/1–014506/11
59. Mezer A, Friedman R, Noivirt O, Nachliel E, Gutman M (2005) *J Phys Chem A* 109:11379–11378
60. Friedman R, Fischer S, Nachliel E, Scheiner S, Gutman M (2007) *J Phys Chem B* 111:6059–6070
61. Wang S, Smith SC (2006) *J Phys Chem B* 110:5084–5093
62. Sakota K, Komoto Y, Nakagaki M, Ishikawa W, Sekiya H (2007) *Chem Phys Lett* 435:1–4
63. Tanner C, Thut M, Steinlin A, Manca C, Leutwyler S (2006) *J Phys Chem A* 110:1758–1766
64. Agmon N (2007) *J Phys Chem B* 111:7870–7878
65. Mente S, Frankland CJV, Reynolds L, Maroncelli M (1998) *Chem Phys Lett* 293:515–522
66. Yokoyama H, Watanabe H, Omi T, Ishiuchi SI, Fujii M (2001) *J Phys Chem A* 105:9366–9374
67. Taketsugu T, Yagi K, Gordon MS (2005) *Int J Quant Chem* 104:758–772
68. Smedarchina Z, Siebrand W, Fernández-Ramos A, Gorb L, Leszczynski J (2000) *J Chem Phys* 112:566–573
69. Gordon MS (1996) *J Phys Chem* 100:3974–3979
70. Fernández-Ramos A, Smedarchina Z, Siebrand W, Zgierski MZ, Rios MA (1999) *J Am Chem Soc* 121:6280–6289
71. Shukla MK, Mishra PC (1998) *Chem Phys* 230:187–200
72. Casadesús R, Moreno M, Lluch JM (2003) *Chem Phys* 290:319–336
73. Chaban GM, Gordon MS (1999) *J Phys Chem A* 103:185–189
74. Fernández-Ramos A, Smedarchina Z, Siebrand W, Zgierski MZ (2001) *J Chem Phys* 114:7518–7526
75. Svartsov YN, Schmitt M (2008) *J Chem Phys* 128:214310/1–214310/9
76. Vu TBC, Kalkman I, Meerts WL, Svartsov YN, Jacoby C, Schmitt M (2008) *J Chem Phys* 128:214311/1–214311/10
77. Koizumi Y, Juvet C, Norihiro T, Ishiuchi SI, Dedonder-Lardeux C, Fujii M (2008) *J Chem Phys* 129:104311/1–104311/10
78. Sakota K, Kageura Y, Sekiya H (2008) *J Chem Phys* 129:054303/1–054303/10
79. Hu WP, You RM, Yen SY, Hung FT, Chou PH, Chou PT (2003) *Chem Phys Lett* 370:139–146
80. Hung FT, Hu WP, Chou PT (2001) *J Phys Chem A* 105:10475–10482
81. Chou PT, Wei CY, Chang CP, Meng-Shin K (1995) *J Phys Chem* 99:11994–12000
82. Herbich J, Hung CY, Thummel RP, Waluk J (1996) *J Am Chem Soc* 118:3508–3518
83. Kyrychenko A, Stepanenko Y, Waluk J (2000) *J Phys Chem A* 104:9542–9555
84. Nosenko Y, Kunitski M, Thummel RP, Kyrychenko A, Herbich J, Waluk J, Riehn C, Brutschy B (2006) *J Am Chem Soc* 128:10000–10001
85. Nosenko Y, Kyrychenko A, Thummel RP, Waluk J, Brutschy B, Herbich J (2007) *Phys Chem Chem Phys* 9:3276–3285
86. Weigend F, Häser M, Patzelt H, Ahlrichs R (1998) *Chem Phys Lett* 294:143–152

87. Schäfer A, Huber C, Ahlrichs R (1994) *J Chem Phys* 100:5829–5835
88. Manca C, Tanner C, Leutwyler S (2005) *Int Rev Phys Chem* 24:457–488
89. Mente S, Maroncelli M (1998) *J Phys Chem A* 102:3860–3876
90. Scott WRP, Hünenberger PH, Tironi IG, Mark AI, Billeter SR, Fennen J, Torda AE, Huber T, Krüger P, van Gunsteren WF (1999) *J Phys Chem A* 103:3596–3607
91. Sobolewski AL, Domcke W, Dedonder-Lardeux C, Jouvet C (2002) *Phys Chem Chem Phys* 4:1093–1100
92. Sobolewski AL, Domcke W (2007) *J Phys Chem A* 111:11725–11735
93. Rode MF, Sobolewski AL (2008) *Chem Phys* 347:413–421
94. Lan Z, Frutos LM, Sobolewski AL, Domcke W (2008) *Proc Natl Acad Sci USA* 105:12707–12712
95. Yau WM, Wimley WC, Gawrisch K, White SH (1998) *Biochemistry* 37:14713–14718
96. Grossfield A, Woolf TB (2002) *Langmuir* 18:198–210
97. Gaede HC, Yau WM, Gawrisch K (2005) *J Phys Chem B* 109:13014–13023
98. Smirnov AV, English DS, Rich RL, Lane J, Teyton L, Schwabacher AW, Luo S, Thornburg RW, Petrich JW (1997) *J Phys Chem B* 101:2758–2769
99. Kyrychenko A, Waluk J (2008) *Biophys Chem* 136:128–135
100. Tieleman DP, Berendsen HJC (1996) *J Chem Phys* 105:4871–4880
101. Tieleman DP, Marrink SJ, Berendsen HJC (1997) *Biochim Biophys Acta* 1331:235–270
102. Rodríguez-Prieto F, Mosquera M, Novo M (1990) *J Phys Chem* 94:8536–8542
103. Mukherjee TK, Ahuja P, Koner AL, Datta A (2005) *J Phys Chem A* 109:12567–12573
104. Mukherjee TK, Panda D, Datta A (2005) *J Phys Chem A* 109:18895–18901
105. Ulander J, Haymet ADJ (2003) *Biophys J* 85:3475–3484
106. Milhaud J (2004) *Biochim Biophys Acta* 1663:19–51
107. Berkowitz ML, Bostick BL, Pandit S (2006) *Chem Rev* 106:1527–1539
108. Kwon OH, Jang DJ (2005) *J Phys Chem B* 109:20479–20484
109. Kyrychenko A, Herbich J, Wu F, Thummel RP, Waluk J (2000) *J Am Chem Soc* 122:2818–2827
110. Kyrychenko A, Waluk J (2003) *J Chem Phys* 119:7318–7327
111. Kyrychenko A, Gorski A, Waluk J (2004) *J Chem Phys* 121:12017–12025
112. Kyrychenko A, Waluk J (2005) *J Chem Phys* 123:064706/1–064706/10
113. Kyrychenko A, Gawinkowski S, Urbańska N, Pietraszkiewicz M, Waluk J (2007) *J Chem Phys* 127:134501/1–134501/12

Kinetics and Dynamics

From Nano- to Bio-Scale

Paneth, P.; Dybala-Defratyka, A. (Eds.)

2010, XVIII, 530 p., Hardcover

ISBN: 978-90-481-3033-7